Available online at www.sciencedirect.com
SCIENCE DIRECT®
Journal of Solid State Chemistry 179 (2006) 2310–2328
JOURNAL OF SOLID STATE CHEMISTRY
www.elsevier.com/locate/jssc

Mn_5Si_3-type host-interstitial boron rare-earth metal silicide compounds RE_5Si_3: Crystal structures, physical properties and theoretical considerations

Jérome Roger[a], Mouna Ben Yahia[a], Volodymyr Babizhetskyy[a,b], Joseph Bauer[a], Stéphane Cordier[a], Roland Guérin[a], Kurt Hiebl[c,**], Xavier Rocquefelte[a,d], Jean-Yves Saillard[a], Jean-François Halet[a,*]

[a]*Sciences Chimiques de Rennes, UMR 6226 CNRS-Université de Rennes 1, Avenue du Général Leclerc, F-35042 Rennes cedex, France*
[b]*Max-Planck-Institute für Festkörperforschung, Heisenbergstrasse 1, Postfach 800665, D-70569 Stuttgart, Germany*
[c]*Innovative Materials Group, Universität Wien, Währingerstrasse 42, A-1090 Wien, Austria*
[d]*Institut des Matériaux Jean Rouxel, Laboratoire de Chimie des Solides, 2 rue de la Houssinière, BP 32229, F-44322 Nantes cedex 3, France*

Received 15 February 2006; received in revised form 14 April 2006; accepted 19 April 2006
Available online 28 April 2006

Dedicated to H.-G. von Schnering on the occasion of his 75th birthday and in recognition of his important contribution to solid state chemistry

Abstract

A series of binary rare-earth metal silicides RE_5Si_3 and ternary boron-interstitial phases $RE_5Si_3B_x$ (RE = Gd, Dy, Ho, Lu, and Y) adopting the Mn_5Si_3-type structure, have been prepared from the elemental components by arc melting. Boron "stuffed" phases were subsequently heated at 1750 K within a high-frequency furnace. Crystal structures were determined for both binary and ternary series of compounds from single-crystal X-ray data: hexagonal symmetry, space group $P6_3/mcm$, $Z = 2$. Boron insertion in the host binary silicides results in a very small decrease of the unit cell parameters with respect to those of the binaries. According to X-ray data, partial or nearly full boron occupancy of the interstitial octahedral sites in the range 0.6–1 is found. The magnetic properties of these compounds were characterized by the onset of magnetic ordering below 100 K. Boron insertion induces a modification of the transition temperature and θ_p values in most of the antiferromagnetic binary silicides, with the exception of the ternary phase $Er_5Si_3B_x$ which was found to undergo a ferromagnetic transition at 14 K. The electrical resistivities for all binary silicides and ternary boron-interstitial phases resemble the temperature dependence of metals, with characteristic changes of slope in the resistivity curves due to the reduced electron scattering in the magnetically ordered states. Zintl–Klemm concept would predict a limiting composition $RE_5Si_3B_{0.6}$ for a valence compound and should then preclude the stoichiometric formula RE_5Si_3B. Density functional theory calculations carried out on some $RE_5Si_3Z_x$ systems for different interstitial heteroatoms Z and different x contents from 0 to 1 give some support to this statement.
© 2006 Elsevier Inc. All rights reserved.

Keywords: Rare-earth metal silicides; Boron insertion; Crystal structure; Magnetic properties; Electrical resistivity; Density functional calculations; Mn_3Si_5-type phases

1. Introduction

With the impetus of Corbett and others, the chemistry of M_5X_3 compounds and their interstitial derivatives $M_5X_3Z_x$ adopting the Mn_5Si_3-type structure [1] is by now largely documented (see for example [2]). Nearly 200 binaries crystallize in this structural type for M from the alkaline-earth, rare-earth or early transition metal groups and X from the main-group element families. One pertinent feature of this structure, which is based on quasi-infinite and inter-bridged M_3X_3 chains composed of confacial octahedra on which separate M atoms bridge the edges of the shared faces, is that a variety of hetero-atoms Z (main-

**Also to be corresponded.
*Corresponding author. Fax: +33 2 23 23 68 40.
E-mail addresses: Kurt.Hiebl@univie.ac.at (K. Hiebl), halet@univ-rennes1.fr (J.-F. Halet).

0022-4596/$ - see front matter © 2006 Elsevier Inc. All rights reserved.
doi:10.1016/j.jssc.2006.04.023

group elements but also transition metals), if not all, may also be found in the centers of the octahedra without any change in lattice type. About 300 of these "stuffed" ternary compounds, often incorrectly labelled Nowotny phases based on pioneering work of Nowotny and co-workers in the late 1950s [3], have been characterized. The Mn_5Si_3-type arrangement is an attractive structure type in which chemical versatilities allow the exploration of a particularly wide range of electronic counts. Indeed, the host lattice has proven to be electronically very tolerant, leading to either semi-conducting or metallic properties often rationalized using Zintl–Klemm concepts [4].

Boron-stuffed Mn_5Si_3-type compounds are rather scarce [2,5–7]. During our investigations of the *RE*–Si–B systems (*RE* = Nd, Gd, Dy, Ho, Er, and Y) at 1270 K, a series of hexagonal phases $RE_5Si_3B_x$ ($x \leqslant 1$) of Mn_5Si_3-type was found in addition to the line compounds $RE_5Si_2B_8$ [8]. These phases result from boron insertion in the octahedral holes of the Mn_5Si_3-type host lattice of the binary silicides RE_5Si_3. Earlier work performed by Mayer et al. [5] mentioned some boron-interstitial phases $RE_5Si_3B_x$ with *RE* = Nd, Gd, Tb, and Dy on the basis of X-ray powder diffraction measurements. It has been shown that insertion of Z elements generally induces some slight increase of the cell volume with respect to that of the host binary compound, except for small main-group elements such as O and N, where some contraction of the unit cell is observed [6]. Mayer et al. could not conclude unambiguously on the variations of the unit cell parameters after boron insertion in the host lattice. Indeed, the unit cell parameters were found to be constant until the atomic composition RE_5Si_3B is attained and then slightly decrease for higher boron content up to $RE_5Si_3B_2$ [6]. Since the octahedral holes cannot accommodate more than one boron atom per formula RE_5Si_3, the authors proposed that beyond RE_5Si_3B, the additional boron atoms could most probably replace Si atoms in the structure, inducing a decrease of the unit cell constants with regard to the smaller atomic radius of boron (0.83 Å) compared to that of silicon (1.17 Å) [9]. It is evident that the exact content of boron and the metric changes cannot be obtained only on the basis of X-ray powder diffraction measurements.

In order to define clearly the boron content and gain metric details in the phases $RE_5Si_3B_x$ which we have evidenced, X-ray single crystal structures for both the binary silicides RE_5Si_3 and the corresponding ternary boron-interstitial phases $RE_5Si_3B_x$ were determined. In addition to the determination of the boron content for each rare-earth metal compound considered, variations of the unit cell parameters as well as residual electron density and interatomic distances for the binary and the ternary compounds can easily be compared. We have succeeded in preparing single crystals of the binary and ternary phases for *RE* = Gd, Dy, Ho, and Y. In the case of *RE* = Nd, Tb, and Er, the boron interstitial phases were observed by electron probe microanalyses and X-ray diffraction (XRD) powder patterns, as well. However, no single crystals could be obtained. With *RE* = Lu, the single crystal structure of the ternary phase $Lu_5Si_3B_x$ could be determined only.

This paper deals with the crystal structures of binary and ternary members of the $RE_5Si_3B_x$ series (*RE* = Gd, Dy, Ho, and Y) as well as that of $Lu_5Si_3B_x$. The influence of boron insertion on the magnetic and electrical properties for the members with *RE* = Gd, Tb, Dy, Ho, and Er is discussed. Finally, results of density functional theory (DFT) calculations performed on the Gd-containing compounds are described in order to gain additional understanding of the bonding in these phases. A preliminary account of some of this work has been published [10].

2. Experimental

2.1. Synthesis

Polycrystalline samples were prepared at room temperature from pure elements: rare-earth metal as ingots (purity > 99.9%), silicon (> 99.99%) and boron (> 99%) as powders, all supplied by Strem Chemicals. Suitable amounts of powder and freshly filed chips of rare-earth metal (the initial molar ratios *RE*/Si/B were close to 5/3/1) were mixed together and pressed into pellets. Arc melting of the samples (800 mg each) was performed on a water-cooled copper hearth under a purified argon atmosphere with a Ti/Zr alloy as a getter. To ensure homogeneity, the samples were turned over and re-melted several times. In the case of the ternary boron-interstitial phases, the samples were introduced, in a second step, in arc-welded sealed tantalum crucibles under 0.5 atmosphere of argon, and then heated up to 1750 K for 3 h with the help of a high-frequency furnace. In all cases, the samples were re-annealed in silica tubes at 1270 K during 15 days and then slowly cooled to room temperature. The molten buttons show a metallic luster and are unreactive towards air.

Platelet-like single crystals of all the binary RE_5Si_3 and ternary $RE_5Si_3B_x$ compounds (*RE* = Gd, Dy, Ho, and Y) were obtained by crushing the solidified samples. Energy dispersive spectroscopy (EDS) and wavelength dispersive spectroscopy (WDS) using scanning electron microscopy (Jeol JSM-6400) and electron microprobe analysis (Camebax SX 50) confirmed rare-earth metal, silicon, and boron as the only components in the samples. A small part of each sample was pulverized and analyzed by XRD using a powder diffractometer (CPS 120 INEL) equipped with a position-sensitive detector ranging from 6° to 120° in 2θ.

2.2. X-ray studies

Single-crystal intensity data for all the binary and ternary phases were collected at ambient temperature using a Nonius Kappa CCD X-ray area-detector diffractometer with graphite-monochromatized Mo$K\alpha$ radiation ($\lambda = 0.71073$ Å). Data collection strategy was performed with the help of the program COLLECT [11] and

reflections were corrected using the program DENZO of the Kappa CCD software package [12]. A numerical absorption correction was applied for all the single crystals on the basis of an optimized description of the crystal faces using the Multiscan program [13]. Structures were solved by direct methods (SIR 97) [14] and least-squares refinements, difference Fourier syntheses were run with SHELXL-97 [15] program package. The program DIAMOND [16] was used for the drawings of the crystal structures. Experimental details and crystallographic data are summarized in Tables 1 and 2.

The crystal structures were solved in the centrosymmetric space group $P6_3/mcm$. The rare-earth and silicon atoms were placed in the crystallographic positions 4*d* and 6*g* in accord with the Mn_5Si_3-type structure. After several refinement cycles with isotropic thermal displacements, the difference Fourier syntheses for the ternary compounds enabled us to localize the boron atoms at the origin of the hexagonal unit cell corresponding to the position 2*b*. The boron insertion in this position confirmed that, in the limits of refinement, the boron content depends on the nature of the rare-earth metal. Thereby, the highest boron content $x = 1$ seems to be reached for RE = Dy, Ho and Lu, whereas the x value was found to be about 0.6 for RE = Gd, and Y. In the final refinement cycles introducing anisotropic displacement parameters for the rare-earth metal and the silicon atoms, the difference Fourier syntheses did not reveal any significant electron density peak. The atomic coordinates, isotropic equivalent displacement parameters and selected interatomic distances for the binary and ternary compounds are given in Tables 3–6. We note that in the case of the ternaries $RE_5Si_3B_x$ the isotropic displacement parameter for boron is quite small for x value equal to 1 with respect to values around 0.6. Although not detected by electron microprobe analysis, oxygen contamination of the samples cannot fully be excluded.

2.3. Physical properties measurements

The magnetic properties were measured by use of a Faraday balance (SUS 10) in the temperature range $80\,K < T < 500\,K$ and in external fields up to 1.3 T and a Lake Shore AC susceptometer (AC 7000, $f = 133.3$ Hz, $B_{AC} = 1$ mT) for temperatures $4.2\,K \leqslant T \leqslant 100\,K$). The *dc* magnetization was measured in the temperature range 1.8–100 K and in fields up to 7 T, using a superconducting quantum interference device (SQUID) magnetometer MPMS-*XL* (Quantum Design). Measurements of the electrical resistivity were carried out applying a common four-probe Lake Shore *ac*-resistivity option ($f = 133.3$ Hz, $i = 10$ mA) in the temperature range 4.2–300 K. The alloy buttons were cut into bars of approximately $1\,mm^2 \times 5$ mm using a diamond saw (Bühler Isomet). Electrical contacts were made with commercial silver paint (Degussa, Hanau, Germany) and 25 μm gold wire.

Table 1
Crystallographic data for RE_5Si_3 (RE = Gd, Dy, Ho and Y)

Empirical formula	Y_5Si_3	Gd_5Si_3	Dy_5Si_3	Ho_5Si_3
Molecular weight	528.8(1)	870.6(1)	896.8(1)	908.9(1)
Crystal system	Hexagonal	Hexagonal	Hexagonal	Hexagonal
Space group	$P6_3/mcm$ (No. 193)	$P6_3/mcm$ (No. 193)	$P6_3/mcm$ (No. 193)	$P6_3/mcm$ (No. 193)
Crystal size (mm^3)	$0.031 \times 0.030 \times 0.028$	$0.140 \times 0.080 \times 0.040$	$0.041 \times 0.037 \times 0.030$	$0.030 \times 0.025 \times 0.013$
a (Å)	8.4096(4)	8.5133(2)	8.3953(2)	8.3533(2)
c (Å)	6.3437(3)	6.4206(3)	6.3138(2)	6.2800(2)
V (Å^3)	388.53(3)	403.00(2)	385.39(2)	379.50(2)
Calculated density ($g\,cm^{-3}$); Z	4.566(1); 2	7.174(1); 2	7.728(1); 2	7.954(1); 2
Linear absorption coefficient (mm^{-1})	37.29	40.91	48.23	51.88
Absorption correction method (T_{min}; T_{max})	Multiscan 0.2831; 0.3704	—	Multiscan 0.1788; 0.2841	Multiscan 0.1861; 0.4008
θ range (deg)	$4.8 \leqslant \theta \leqslant 32.5$	$4.8 \leqslant \theta \leqslant 30$	$4.8 \leqslant \theta \leqslant 30$	$4.8 \leqslant \theta \leqslant 32$
h	$-10 \leqslant h \leqslant 12$	$-11 \leqslant h \leqslant 11$	$-11 \leqslant h \leqslant 11$	$-9 \leqslant h \leqslant 12$
k	$-12 \leqslant k \leqslant 12$	$-9 \leqslant k \leqslant 9$	$-11 \leqslant k \leqslant 11$	$-12 \leqslant k \leqslant 10$
l	$-9 \leqslant l \leqslant 8$	$-9 \leqslant l \leqslant 8$	$-8 \leqslant l \leqslant 8$	$-9 \leqslant l \leqslant 9$
Refinement method	SHELXL; F^2	SHELXL; F^2	SHELXL; F^2	SHELXL; F^2
Reflections collected	5657	1388	4517	4992
Independent reflections; R_{int}	274; 0.066	234; 0.052	223; 0.061	266; 0.035
Reflections in refinement ($I > 2\sigma(I)$)	248	228	222	247
Number of variables	12	12	12	12
R ($I > 2\sigma(I)$); wR_2	0.032; 0.074	0.029; 0.082	0.017; 0.047	0.011; 0.027
R (all data); wR_2	0.036; 0.076	0.029; 0.082	0.017; 0.047	0.013; 0.028
Goodness-of-fit on F^2	1.03	1.04	1.03	1.01
Extinction coefficient	0.0040(18); Shelxl	0.0036(9); Shelxl	0.0021(4); Shelxl	0.0004(2); Shelxl
$\Delta\rho$ (min, max) (e/Å^3)[a]	−1.16/+3.54	−2.06/+4.03	−1.08/+3.77	−0.54/+3.70

Unit cell parameters from powdered samples for Nd_5Si_3: $a = 8.671(1)$ Å, $c = 6.577(2)$ Å; Tb_5Si_3: $a = 8.456(2)$ Å, $c = 6.352(2)$ Å; Er_5Si_3: $a = 8.297(1)$ Å, $c = 6.220(1)$ Å.

[a]Smallest and largest residual electron density found in the area of the rare-earth metal positions.

Table 2
Crystallographic data for $RE_5Si_3B_x$ (RE = Gd, Dy, Ho, Lu and Y)

Empirical formula	$Y_5Si_3B_{0.65}$	$Gd_5Si_3B_{0.6}$	$Dy_5Si_3B_1$	$Ho_5Si_3B_1$	$Lu_5Si_3B_1$
Molecular weight	535.8(1)	877.0(1)	907.6(1)	919.7(1)	969.9(1)
Crystal system	Hexagonal	Hexagonal	Hexagonal	hexagonal	hexagonal
Space group	$P6_3/mcm$ (No. 193)	$P6_3/mcm$ (No. 193)	$P6_3/mcm$ (No. 193)	$P6_3/mcm$ (No. 193)	$P6_3/mcm$ (No. 193)
Crystal size (mm^3)	$0.030 \times 0.020 \times 0.020$	$0.040 \times 0.038 \times 0.031$	$0.035 \times 0.027 \times 0.020$	$0.034 \times 0.030 \times 0.014$	$0.031 \times 0.027 \times 0.018$
a (Å)	8.4033(4)	8.5055(2)	8.3675(2)	8.3317(2)	8.1746(4)
c (Å)	6.3351(3)	6.4172(2)	6.2594(2)	6.2392(2)	6.0908(4)
V (Å^3)	387.42(3)	402.05(2)	379.54(2)	375.08(2)	352.48(3)
Calculated density ($g\,cm^{-3}$); Z	4.580(1); 2	7.280(1); 2	7.942(1); 2	8.096(1); 2	9.088(1); 2
Linear absorption coefficient (mm^{-1})	37.39	41.01	48.98	52.49	69.75
Absorption method	Multiscan	Multiscan	Multiscan	Multiscan	Multiscan
(T_{min}; T_{max})	0.2241; 0.5247	0.1647; 0.2956	0.3448; 0.6676	0.2618; 0.6032	0.2092; 0.3381
θ range (deg)	$4.8 \leqslant \theta \leqslant 37.5$	$4.8 \leqslant \theta \leqslant 37.5$	$4.8 \leqslant \theta \leqslant 37.4$	$2.8 \leqslant \theta \leqslant 36.5$	$5.0 \leqslant \theta \leqslant 32$
h	$-12 \leqslant h \leqslant 14$	$-9 \leqslant h \leqslant 14$	$-12 \leqslant h \leqslant 14$	$-13 \leqslant h \leqslant 13$	$-11 \leqslant h \leqslant 12$
k	$-14 \leqslant k \leqslant 13$	$-14 \leqslant k \leqslant 13$	$-14 \leqslant k \leqslant 11$	$-13 \leqslant k \leqslant 13$	$-12 \leqslant k \leqslant 12$
l	$-10 \leqslant l \leqslant 10$	$-10 \leqslant l \leqslant 10$	$-10 \leqslant l \leqslant 10$	$-10 \leqslant l \leqslant 5$	$-9 \leqslant l \leqslant 9$
Refinement method	SHELXL; F^2	SHELXL; F^2	SHELXL; F^2	SHELXL ; F^2	SHELXL ; F^2
Reflections collected	6371	7996	6679	6229	5043
Independent reflections; R_{int}	391; 0.079	415; 0.058	392; 0.066	365; 0.058	244; 0.072
Reflections in refinement ($I>2\sigma(I)$)	323	380	352	335	212
Number of variables	14	14	13	13	13
R ($I>2\sigma(I)$); wR_2	0.024; 0.027	0.025; 0.093	0.020; 0.058	0.022; 0.052	0.025; 0.052
R (all data); wR_2	0.039; 0.029	0.030; 0.097	0.025; 0.060	0.025; 0.053	0.037; 0.055
Goodness-of-fit on F^2	1.00	1.05	1.04	1.03	1.00
Extinction coefficient	0.0014(4); Shelxl	0.0037(8); Shelxl	0.0013(4); Shelxl	0.0067(5); Shelxl	0.0002(1); Shelxl
$\Delta\rho$ (min, max) (e/Å^3)[a]	−0.58/+0.95	−1.95/+1.39	−1.29/+1.60	−2.07/+2.83	−2.43/+1.88

Unit cell parameters from powdered samples for $Nd_5Si_3B_x$: $a = 8.665(2)$ Å, $c = 6.526(2)$ Å; $Tb_5Si_3B_x$: $a = 8.427(2)$ Å, $c = 6.332(2)$ Å; $Er_5Si_3B_x$: $a = 8.279(1)$ Å, $c = 6.198(1)$ Å.

[a]Smallest and largest residual electron density found in the area of the rare-earth metal positions.

Table 3
Atomic positional and isotropic displacement parameters for RE_5Si_3 (RE = Gd, Dy, Ho and Y)

	Site		Y_5Si_3	Gd_5Si_3	Dy_5Si_3	Ho_5Si_3
*RE*1	4*d*	x	1/3	1/3	1/3	1/3
		y	2/3	2/3	2/3	2/3
		z	0	0	0	0
		U_{eq}	0.0125(3)	0.0112(3)	0.0124(2)	0.0087(1)
*RE*2	6*g*	x	0.2402(1)	0.2424(1)	0.2409(1)	0.2401(1)
		y	0	0	0	0
		z	1/4	1/4	1/4	1/4
		U_{eq}	0.0131(2)	0.0096(3)	0.0110(2)	0.0083(1)
Si	6*g*	x	0.6040(2)	0.6047(4)	0.6035(3)	0.6038(2)
		y	0	0	0	0
		z	1/4	1/4	1/4	1/4
		U_{eq}	0.0129(4)	0.0094(7)	0.0100(5)	0.0082(3)

2.4. Theoretical calculations

Electronic density of states (DOS) were calculated for Gd_5Si_3 and $Gd_5Si_3B_x$ ($x = 2/3$ and 1) with the tight-binding linear muffin-tin orbital (LMTO) method including the combined correction in the atomic spheres approximation (ASA) using the TB–LMTO–ASA program package [17]. Exchange and correlation were treated in the local density approximation using the von Barth–Hedin local exchange correlation potential [18]. Empty spheres (ES) were introduced in the last to achieve space filling. The optimal positions and radii of these additional ES were determined automatically. The full LMTO basis set consisted of 6*s*, 6*p*, 5*d* and 4*f* functions for Gd spheres, 3*s*, 3*p*, and 3*d* functions for Si spheres, 2*s*, 2*p* and 3*d* functions for B spheres and *s*, *p* and *d* functions for ES. The eigenvalue problem was solved using the following minimal basis set obtained from Löwdin downfolding technique: Gd (4*f*, 5*d*, 6*s*), Si (3*s*, 3*p*), B (2*s*, 2*p*), and ES (1*s*). The k space integration was performed using the tetrahedron method [19]. 21 irreducible k points were taken for the calculations. The DOS curves have been shifted in order that the Fermi level lies at 0 eV. The crystal structures of Gd_5Si_3 and $Gd_5Si_3B_{0.6}$ were used for the calculations using a supercell $a' \times b' \times c$ ($a' = b' = \sqrt{3}a$).

Full optimizations of the atomic positions and cell parameters were carried out on $Gd_5Si_3B_x$ within the supercell defined above for different boron contents, 1/3,

Table 4
Atomic positional and isotropic displacement parameters for $RE_5Si_3B_x$ (RE = Gd, Dy, Ho, Lu and Y)

	Site		$Y_5Si_3B_{0.65}$	$Gd_5Si_3B_{0.60}$	$Dy_5Si_3B_1$	$Ho_5Si_3B_1$	$Lu_5Si_3B_1$
*RE*1	*4d*	*x*	1/3	1/3	1/3	1/3	1/3
		y	2/3	2/3	2/3	2/3	2/3
		z	0	0	0	0	0
		U_{eq}	0.0079(1)	0.0129(2)	0.0103(2)	0.0097(2)	0.0067(2)
*RE*2	6*g*	*x*	0.2390(1)	0.2410(1)	0.2355(1)	0.2340(1)	0.2337(1)
		y	0	0	0	0	0
		z	1/4	1/4	1/4	1/4	1/4
		U_{eq}	0.0087(1)	0.0114(2)	0.0096(2)	0.0093(2)	0.0070(2)
Si	6*g*	*x*	0.6031(1)	0.6031(3)	0.6015(3)	0.6010(2)	0.6011(5)
		y	0	0	0	0	0
		z	1/4	1/4	1/4	1/4	1/4
		U_{eq}	0.0082(2)	0.0121(5)	0.0107(4)	0.0090(3)	0.0073(8)
B	*2b*	*x*	0	0	0	0	0
		y	0	0	0	0	0
		z	0	0	0	0	0
		U_{iso}	0.032(4)	0.050(8)	0.009(2)	0.007(2)	0.007(5)
		τ[a]	0.65(3)	0.60(7)	1	1	1

[a]Occupation number.

Table 5
Selected interatomic distances (Å) for RE_5Si_3 (RE = Gd, Dy, Ho and Y)

	Y_5Si_3	Gd_5Si_3	Dy_5Si_3	Ho_5Si_3
*RE*1				
6Si	3.029(1)	3.068(1)	3.020(1)	3.006(1)
2*RE*1	3.172(1)	3.210(2)	3.157(1)	3.140(1)
6*RE*2	3.631(1)	3.664(4)	3.619(1)	3.605(1)
*RE*2				
2Si	2.906(2)	2.939(2)	2.905(2)	2.888(2)
1Si	3.060(2)	3.084(3)	3.044(2)	3.038(2)
2Si	3.432(1)	3.464(1)	3.417(1)	3.400(1)
2*RE*2	3.499(1)	3.574(1)	3.502(1)	3.474(1)
4*RE*1	3.631(1)	3.664(4)	3.619(2)	3.605(1)
4*RE*2	3.760(1)	3.816(3)	3.749(1)	3.726(1)
Si				
2*RE*2	2.906(2)	2.939(2)	2.905(2)	2.888(2)
4*RE*1	3.029(1)	3.068(1)	3.020(1)	3.006(1)
1*RE*2	3.060(2)	3.084(3)	3.044(2)	3.038(2)
2*RE*2	3.432(1)	3.464(1)	3.417(1)	3.400(1)

2/3 and 1 using the VASP package [20]. Ions cores were represented by projector-augmented wave pseudopotentials provided within the program [21]. The orbitals La (5*p*, 4*f*, 5*d*, 6*s*), Gd (4*f*, 5*d*, 6*s*), Zr (4*s*, 4*p*, 4*d*, 5*s*), Ge (3*d*, 4*s*, 4*p*), Si and P (3*s*, 3*p*) and B, C, and N (2*s*, 2*p*) were treated as valence states. The Perdew–Burke–Ernzerhof (PBE) generalized gradient approximation (GGA) was employed for the exchange and correlation energy term [22]. The Brillouin zone was sampled using $2 \times 2 \times 4$ Monkhorst-Pack grid. A plane wave basis set with a cut-off energy of 400 eV was used to construct the valence electronic wave functions.

Table 6
Selected interatomic distances (Å) for $RE_5Si_3B_x$ (RE = Gd, Dy, Ho, Lu and Y)

	$Y_5Si_3B_{0.65}$	$Gd_5Si_3B_{0.60}$	$Dy_5Si_3B_1$	$Ho_5Si_3B_1$	$Lu_5Si_3B_1$
*RE*1					
6Si	3.024(1)	3.062(1)	3.001(1)	2.988(1)	2.928(2)
2*RE*1	3.168(1)	3.209(1)	3.130(1)	3.120(1)	3.046(1)
6*RE*2	3.634(1)	3.668(1)	3.631(1)	3.624(1)	3.553(1)
*RE*2					
2B	2.557(1)	2.603(1)	2.517(1)	2.497(1)	2.443(1)
2Si	2.909(1)	2.946(2)	2.904(2)	2.894(2)	2.838(3)
1Si	3.060(1)	3.080(3)	3.062(2)	3.058(2)	3.003(4)
2Si	3.435(1)	3.472(1)	3.414(1)	3.409(1)	3.332(2)
2*RE*2	3.478(1)	3.550(1)	3.414(1)	3.376(1)	3.310(1)
4*RE*1	3.634(1)	3.668(1)	3.631(1)	3.624(1)	3.553(1)
4*RE*2	3.750(1)	3.808(1)	3.698(1)	3.678(1)	3.595(1)
Si					
2*RE*2	2.909(1)	2.946(2)	2.904(2)	2.894(2)	2.838(3)
4*RE*1	3.024(1)	3.062(1)	3.001(1)	2.988(1)	2.928(2)
1*RE*2	3.060(1)	3.080(3)	3.062(2)	3.058(2)	3.003(4)
2*RE*2	3.435(1)	3.472(1)	3.414(1)	3.409(1)	3.332(2)
B					
6*RE*2	2.557(1)	2.603(1)	2.517(1)	2.497(1)	2.443(1)

3. Results and discussion

3.1. Crystal structures

Surprisingly boron insertion causes a slight decrease (0.2–1.5%) of the unit cell volume of the ternaries compared to that of the corresponding binary silicides (Tables 2 and 3). The largest variation occurs for x value equal to one. For instance, the hexagonal unit cell parameters for $Dy_5Si_3B_x$ are $a = 8.3675(2)$ Å, $c = 6.2594(2)$ Å, V = 379.54(2) Å^3, whereas those of the binary silicide Dy_5Si_3 are $a = 8.3953(2)$ Å, $c = 6.3138(2)$ Å, $V = 385.39(2)$ Å^3, i.e., a volume decrease of 1.5%. This result contrasts with some comments in literature, which stipulate that insertion of boron within host binary M_5X_3 structures such as La_5Ge_3 generally induces modest volume increase [6,23].

The structural arrangement of the ternary phase $RE_5Si_3B_x$, common for every rare-earth metal is shown in Fig. 1. The rare-earth metal atoms *RE*1, which are located on the threefold axes at the height $z = 0$ and 1/2, are surrounded by six silicon atoms in a rather complex coordination sphere which can be viewed as a distorted trigonal prism. The rare-earth metal atoms *RE*2 located around the origin of the unit cell, aggregate to form octahedral clusters RE_6 (or "trigonal antiprisms" RE_6) which condense by sharing basal faces along the [001] direction. Boron is incorporated into interstitial sites located at (0, 0, 0) and (0, 0, 0.5) in the middle of the metal octahedra. With two formula units per cell, up to two interstitial boron atoms can be accommodated per unit cell. This yields a formula for the fully occupied structure corresponding to $RE_5Si_3B_{1.0}$. For RE = Dy, Ho, and Lu,

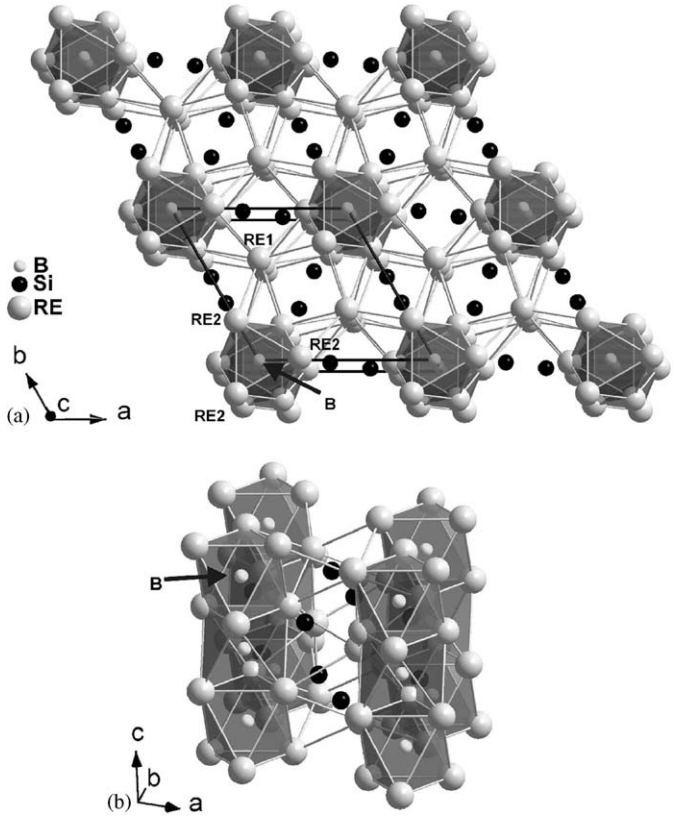

Fig. 1. Crystal structure of the boron-interstitial phase $RE_5Si_3B_x$: (a) down the *c*-axis; (b) along the *c*-axis. The RE_6 octahedra containing the boron atoms are emphasized. The drawing corresponds to full occupancy ($x = 1$) of boron.

this limiting formula seems to be reached whereas for $RE = Gd$, and Y, the site is only 60–65% occupied (Table 4). It is worth mentioning that some stuffed phases have been found with smaller boron content, such as $Ti_5Si_3B_{0.45}$ for example [7].

Incorporation of boron in the interstitial sites within the chains of RE_6 octahedra involves *RE*2–B bonds as suggested by the cavity contraction, although the *RE*2 atoms are now surrounded by seven metalloïd atoms (5Si + 2B) instead of five silicon atoms as in RE_5Si_3. The overall coordination number (CN) of the *RE*2 atoms is therefore CN = 17 for RE_5Si_3B instead of CN = 15 for RE_5Si_3 (Tables 5 and 6). On the contrary, the CN remains equal to 14 for the *RE*1 atoms in both structures, since they are not affected by the additional B atoms. Finally, no metalloid–metalloïd bond occurs in both binary and ternary structures.

A more detailed analysis of the distances shows a slight decrease of the *RE*2–*RE*2 distances within the RE_6 octahedra when boron is present. Indeed, the *RE*2–*RE*2 distances for Dy_5Si_3B for instance (Dy2–2Dy2 and Dy2–4Dy2 within the Dy_6 octahedron, i.e., 3.41 and 3.70 Å, respectively) are smaller than those in Dy_5Si_3 (3.50 and 3.75 Å). Covalent bonding between inserted boron atoms and the surrounded rare-earth metals may explain the slight shrinking of the octahedra and consequently that of the unit cell parameters.

Attempts to obtain single crystals for RE = Nd, Tb, and Er were unsuccessful. However, substantial unit cell variations observed on X-ray powder diffraction patterns with and without boron (see bottom of Tables 1 and 2) as well as qualitative microanalyses by WDS prove unambiguously the existence of the boron interstitial phases $Nd_5Si_3B_x$, $Tb_5Si_3B_x$, and $Er_5Si_3B_x$.

3.2. Magnetic and electrical properties

We point out that all the binary compounds investigated here were intensively studied in the literature before (see Table 7). We mainly concentrated our research on the samples with ternary boron-interstitial phases. The results are presented below. For all samples, the reciprocal mass susceptibility follows a linear Curie–Weiss behavior. The effective magnetic moments μ_{eff} and the corresponding values of the paramagnetic Curie temperatures were calculated by least-squares fits using the modified formula

$$\chi_m = \frac{C}{T - \Theta_p} + \chi_0, \quad (1)$$

where C is the Curie constant, Θ_p the paramagnetic Curie temperature and χ_0 denotes temperature independent contributions such as core diamagnetism, Landau diamagnetism

Table 7
Magnetic and electrical data for the binary and ternary phases RE_5Si_3 and $RE_5Si_3B_x$ (RE = Gd, Tb, Dy, Ho, Er, and Y)

Compound	μ_{eff} (μ_B)	θ_p (K)	T_C (K)	T_N (K)	$(d\rho/dT)_{max}$ (K)	Ref.
Gd_5Si_3	8.2	151		75	75	This work
	7.5	205		(280)		[24]
	8.34	97		62		[25]
				66	77	[26]
	8.5	42		55	78	[27,28]
$Gd_5Si_3B_x$	7.9	132		67	67	This work
Tb_5Si_3	9.4	81		69	68	This work
				50	53	[26]
				73	69	[27]
				50		[29]
$Tb_5Si_3B_x$	9.2	66		67	67	This work
Dy_5Si_3	10.7	84	120	84		This work
	10.4	100	107			[24]
		90				[25]
				24	34	[26]
	10.4	110.8		125		[27]
$Dy_5Si_3B_x$	10.4	100	(120)	54; 84	50; 86	This work
Ho_5Si_3	10.5	16.5	11	25	13; 25	[30]
$Ho_5Si_3B_x$	10.8	23	15		—	This work
Er_5Si_3				15.5		[31]
				20		[32]
$Er_5Si_3B_x$	9.8	27	14	25	—	This work

and Pauli paramagnetism. The derived values for μ_{eff} in Table 7 are in good accord with the theoretical tripositive RE^{3+} free ion moments.

The results for the electrical resistivities $\rho(T)$ versus temperature of the binary and ternary phases are also presented below and the derived constants are listed in Table 7. Some of the results are given relative to the room temperature values ($\rho/\rho_{300\,K}$), because we were not successful in cutting bar-shaped samples due to the brittleness of the compounds. The general features of the $\rho(T)$ curves for all the samples resemble the typical shape of metal-like, magnetically ordered intermetallics. The values of $\rho(T)$ decrease with decreasing temperature with a characteristic change of slope at the magnetic ordering temperatures due to the reduction in scattering of the conduction electrons in the ordered state. In the ordered regime, the data were fitted by using the power law:

$$\rho(T) = \rho_0 + aT^{\alpha}. \quad (2)$$

Gd_5Si_3 and $Gd_5Si_3B_x$: The magnetic measurements of Gd_5Si_3, as presented in Fig. 2, were seriously disturbed by the fact that the polycrystalline samples were always slightly polluted by the strongly ferromagnetic neighbor compound Gd_5Si_4 (ferromagnet with $T_C = 336\,K$) [33]. Our sample undergoes an antiferromagnetic transition at a Néel point $T_N = 75\,K$ indicated by the shallow maxima of both χ' and χ_{dc} plots (upper inset in Fig. 2), although the θ_p value is strongly positive. It has been demonstrated in literature that Gd_5Si_3 does not have a straightforward antiferromagnetic structure. Indeed, magnetization measurements in applied fields up to 12 T at 4.2 K have been interpreted in terms of a helimagnetic ordering gradually changing to a ferromagnetic state with a saturation value $\mu_S = 7\mu_B$ per Gd atom, due to a metamagnetic-like behavior. The isothermal magnetization plot versus field (see lower inset in Fig. 2) at $T = 1.8\,K$ has been corrected for the saturated magnetization data stemming from Gd_5Si_4 impurity and proves the results given in literature. A spin reorientation seems to occur above a critical field $B \sim 4T$.

Boron insertion in the binary compound changes the magnetic behavior of the master alloy in the following manner: In the paramagnetic regime (Fig. 3), we observe a decrease of the paramagnetic Curie temperature θ_p value (Table 7), which suggests that the indirect exchange energy ($\theta_p \propto J_{ex}^2$) is reduced. The value of the effective magnetic moment μ_{eff} is perfectly identical to the theoretical one of $7.9\,\mu_B$. The *ac* susceptibility versus temperature (inset in Fig. 3) proves an antiferromagnetic ordering at $T_N = 67\,K$ (χ' shows a maximum while χ'' is practically temperature independent). The pronounced reduction of $T_N = 67\,K$ for the ternary compound instead of $T_N = 75\,K$ for pure binary sample is certainly due to the volume contraction (oscillating character of the RKKY function) caused by the addition of boron [34]. The isothermal magnetizable versus external field at $T = 2\,K$ (lower inset in Fig. 3) is fully reversible and practically linear up to ~4 T. In higher field, the $M(B)$ curve bends up due to a metamagnetic-like transition, similarly observed for Gd_5Si_3. The ordered moment $\mu_s = 2.6\,\mu_B$ at $B = 5\,T$ is far away from saturation ($7\,\mu_B$/Gd atom).

The resistivity plot $\rho(T)$ of the binary silicide Gd_5Si_3 resembles the typical shape of metal-like, magnetically ordered intermetallics (Fig. 4). The values of $\rho(T)$ decrease with decreasing temperature with a characteristic change of slope at the magnetic ordering temperatures due to the reduction in scattering of the conduction electrons in the ordered state. Indeed, we observe a sharp transition, characterized by a maximum change of slope at $T_N = 75\,K$ in accord with literature data (Table 7). We note that the

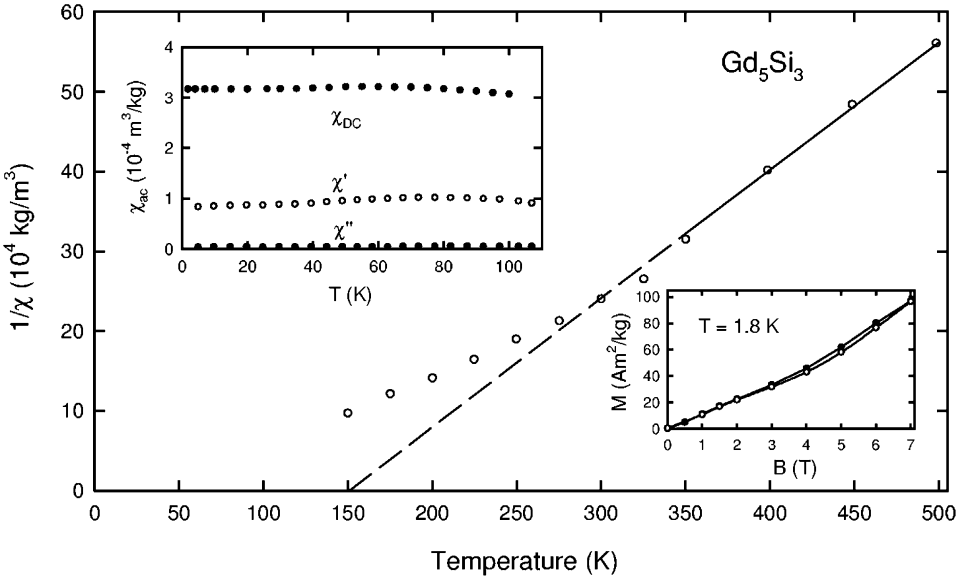

Fig. 2. Reciprocal susceptibility versus temperature for Gd_5Si_3. Upper inset: *ac* susceptibilities versus temperature. Lower inset: isothermal magnetization versus external field (open circles field up, filled symbols field down).

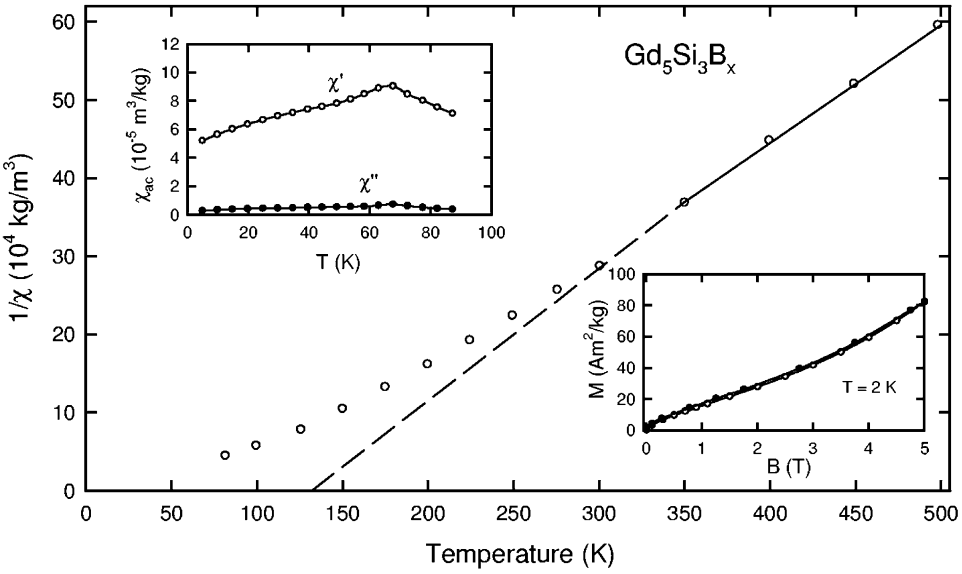

Fig. 3. Reciprocal susceptibility versus temperature for $Gd_5Si_3B_x$. Upper inset: *ac* and *dc* susceptibilities versus temperature. Lower inset: isothermal magnetization versus external field (open circles field up, filled symbols field down).

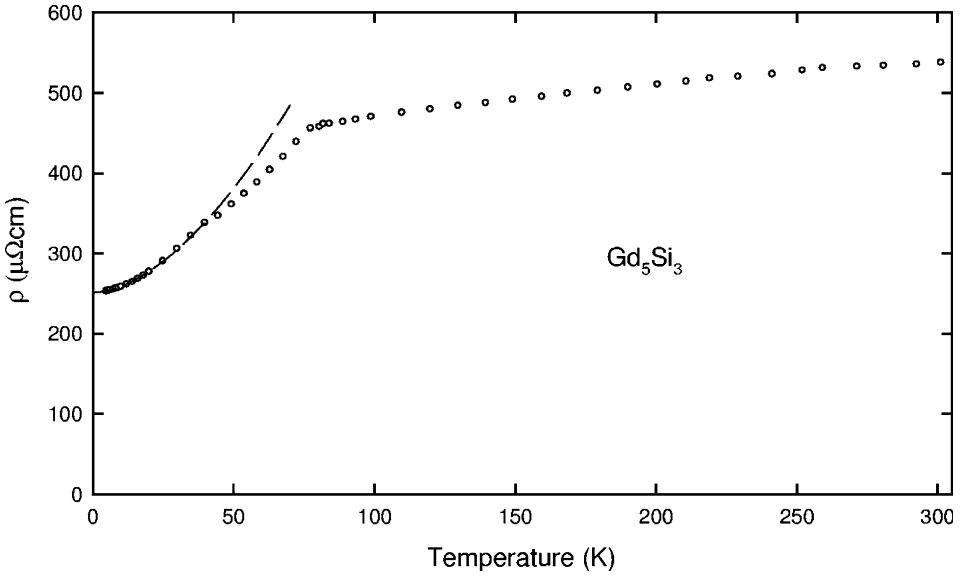

Fig. 4. Electrical resistivity versus temperature for Gd_5Si_3. Dashed line calculated after Eq. (2).

resistivity measurements are less sensitive to the influence of the impurities and hence give a better proof for the onset of the magnetic ordering.

The $\rho(T)$ plot of the boron interstitial phase is less "metallic" than the similar plot of Gd_5Si_3 (Fig. 5). The resistivity is more or less constant in a wide temperature range (300–150 K). Upon lowering the temperature, the ρ values increase due to the "superzone" effects [35] observed in antiferromagnets and are followed by a sharp decrease at $T_N = 67$ K (Fig. 5). A fit according to Eq. (2) results in an even smaller value of $\alpha = 1.3$ ($\alpha = 1.8$ for Gd_5Si_3) instead of $\alpha = 3-4$ as expected for antiferromagnets, which suggests a rather complex spin structure [36].

Tb_5Si_3 and $Tb_5Si_3B_x$: The magnetic properties of Tb_5Si_3 were intensively investigated in literature (see Table 7). However, no data for the paramagnetic regime were presented. The reciprocal susceptibility is plotted versus temperature in Fig. 6. The paramagnetic Curie temperature θ_p is positive and equal to 81 K. The effective moment $\mu_{eff} = 9.4\,\mu_B$ is close to the theoretical tripositive Tb^{3+} free ion moment ($\mu_{eff} = 9.7\,\mu_B$). The *ac* susceptibility χ' shows a pronounced maximum at $T_N = 69$ K, a finding which is in

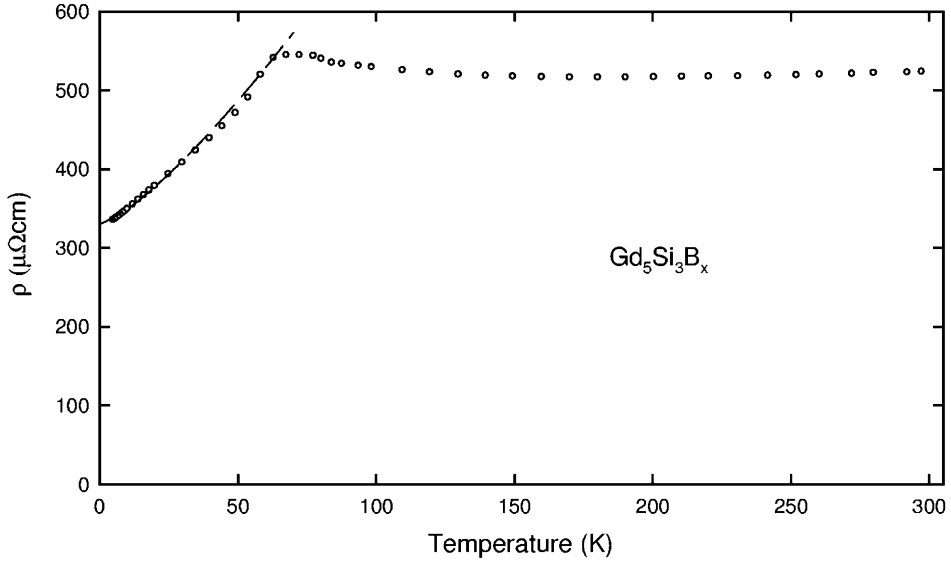

Fig. 5. Electrical resistivity versus temperature for $Gd_5Si_3B_x$. Dashed line calculated after Eq. (2).

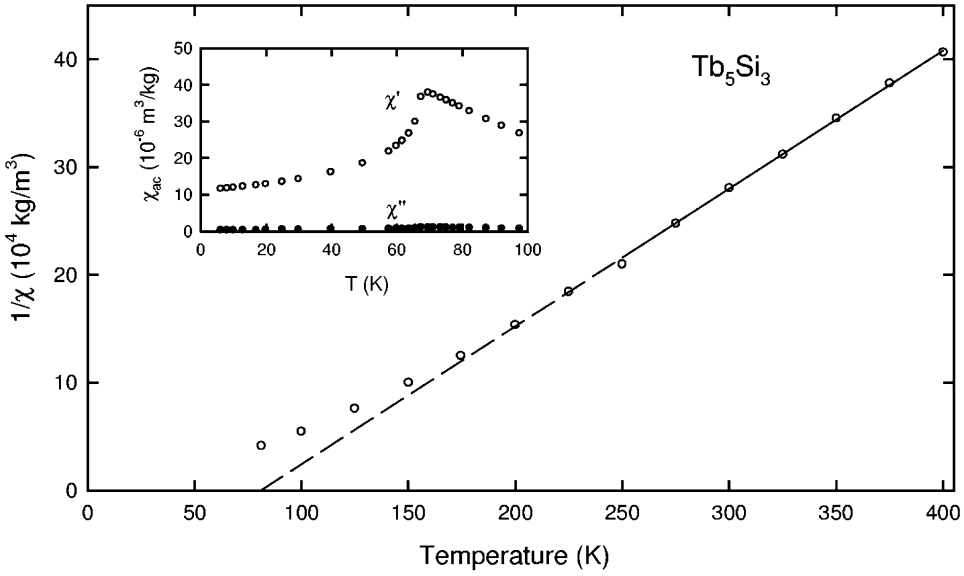

Fig. 6. Reciprocal susceptibility versus temperature for Tb_5Si_3. Inset: *ac* susceptibilities versus temperature.

less accord with the literature data. χ'' is temperature independent proving the antiferromagnetic ground state (inset in Fig. 6).

The electrical resistivity of Tb_5Si_3 decreases weakly down from room temperature due to the metallic state. Below 100 K, a small increase is observed (super-zone scattering) and finally a pronounced change of slope is encountered at $T_N = 68$ K (Fig. 7). The value for $\alpha = 2.7$ (<3) from Eq. (2) is plausible due to the complicated helical spin structure (Tb1 flat spiral, Tb2 conical) as proposed by Semitelou et al. [29].

The reciprocal susceptibility versus temperature for the boron interstitial ternary phase $Tb_5Si_3B_x$ is plotted in Fig. 8. The linear extrapolation of the data leads to a paramagnetic Curie temperature $\theta_p = 66$ K and $\mu_{eff} = 9.2\,\mu_B$ per Tb atom. Similarly, the θ_p value is lower than that of the binary compound, which was already observed in the Gd_5Si_3–B system. The *ac* susceptibility plots (inset in Fig. 8) are quite comparable with those of the binary compound. Again the small volume contraction is probably responsible for the somewhat lower $T_N = 67$ K. Hence, we tend to believe that the boron content within the sample is rather small ($x<0.2$).

The resistivity curve (Fig. 9) is also rather similar to the $\rho(T)$ plot of Tb_5Si_3. However, we note the generally higher ρ values due to the higher porosity of the sample after boron insertion. The small α value $= 2.7$ instead of 3.5 for the binary silicide Tb_5Si_3 tends to prove that the boron insertion reduces the complexity of the magnetic structure [29].

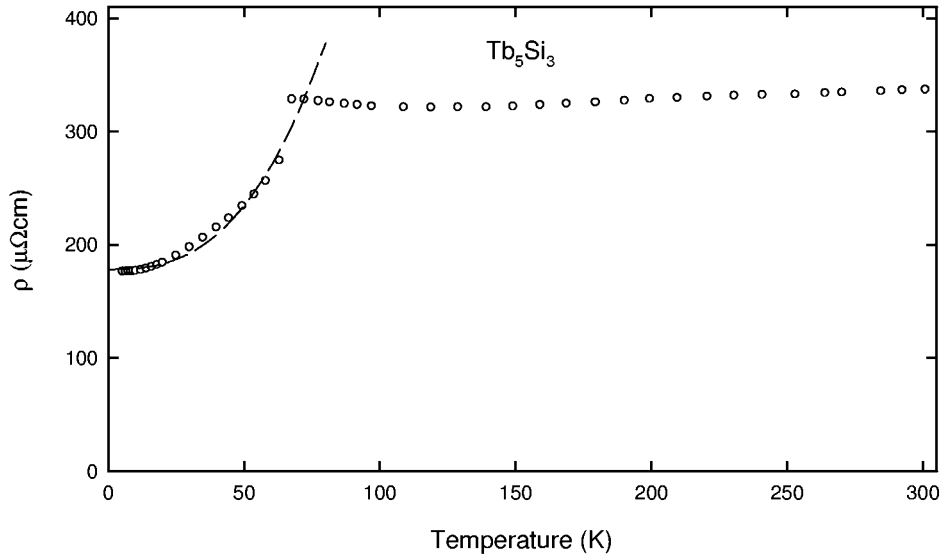

Fig. 7. Electrical resistivity versus temperature for Tb_5Si_3. Dashed line calculated after Eq. (2).

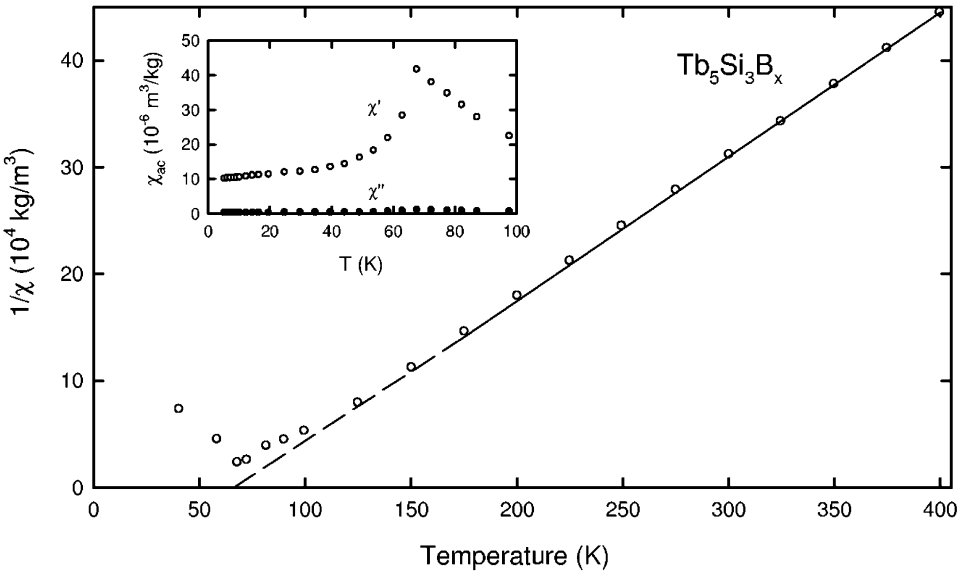

Fig. 8. Reciprocal susceptibility versus temperature for $Tb_5Si_3B_x$. Inset: *ac* susceptibilities versus temperature.

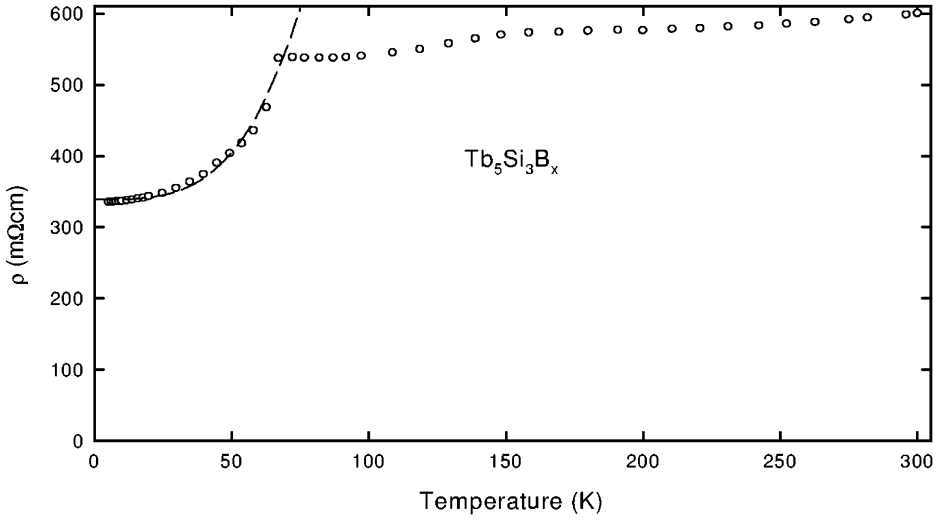

Fig. 9. Electrical resistivity versus temperature for $Tb_5Si_3B_x$. Dashed line calculated after Eq. (2).

Dy_5Si_3 and $Dy_5Si_3B_x$: The binary compound Dy_5Si_3 was also investigated according to the literature [24–27] and the obtained results vary dramatically (see Table 7). Indeed, the magnetic properties seem to be also complicated according to our findings. In the paramagnetic regime (Fig. 10), we derive θ_p and the μ_{eff} values in accord with other authors. The *ac* susceptibility ($B = 1$ mT, upper inset in Fig. 10) plots reveals a χ' maximum at Néel point $T_N = 84$ K followed by shoulders around 70 and 20 K as well as a weak temperature dependence for χ''. This curve is as complicated as that presented by Semitelou et al. for $B = 0.01$ T [37]. However, in a moderate field $B = 0.1$ T, the magnetization curve $M(T)$ changes its feature (upper inset in Fig. 10). As the sample was zero field cooled (ZFC), we observe an increase of $M(T)$ up to 50 K, then followed by a broad plateau. Above 100 K the magnetization decreases rapidly. In the magnetization versus field at 80 K (upper inset in Fig. 10), a ferromagnetic-like behavior is encountered. Indeed, our measurements in the temperature range above 80 K in four different fields (0.75, 0.99, 1.1 and 1.3 T) resulted in a pronounced field dependence below 120 K. Hence, we believe that for this compound a weak ferromagnetism is induced at about $T_C = 120$ K. The isothermal magnetization $M(B)$ at 2 K (lower inset in

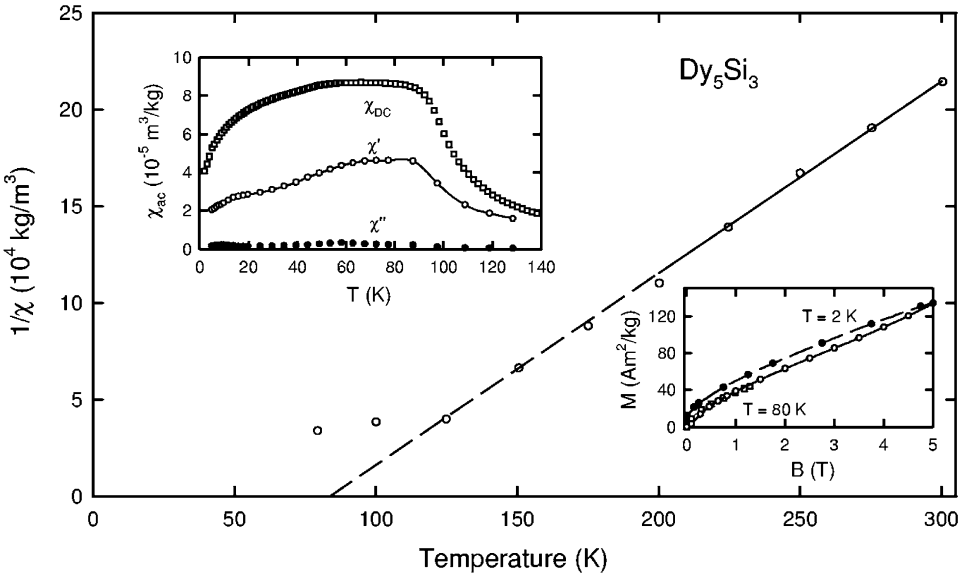

Fig. 10. Reciprocal susceptibility versus temperature for Dy_5Si_3. Upper inset: *ac* and *dc* susceptibilities versus temperature. Lower inset: isothermal magnetization versus external field (open symbols field up, filled symbols field down).

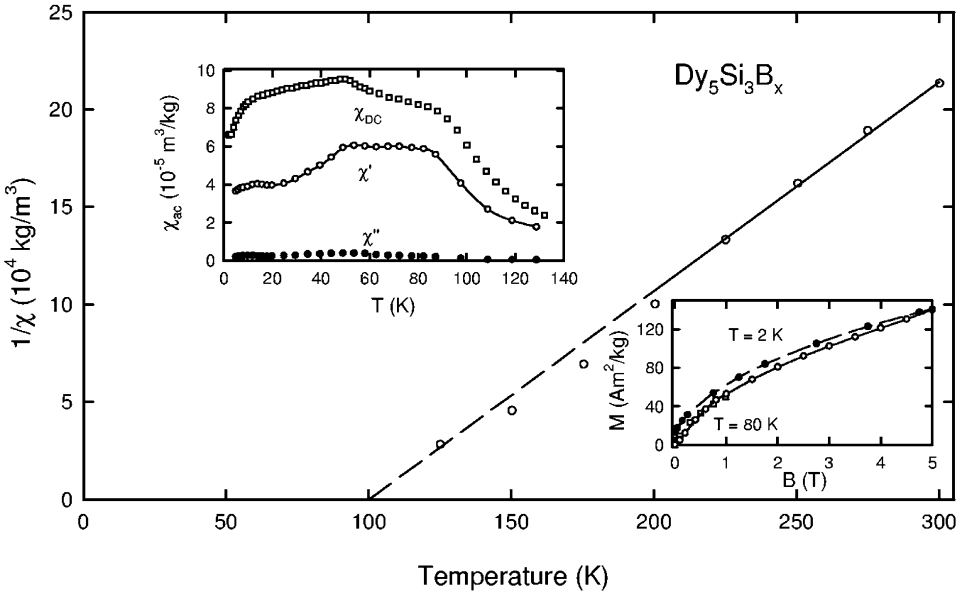

Fig. 11. Reciprocal susceptibility versus temperature for $Dy_5Si_3B_x$. Upper inset: *ac* and *dc* susceptibilities versus temperature. Lower inset: isothermal magnetization versus external field (open symbols field up, filled symbols field down).

Fig. 10) shows a quasi-linear behavior in increasing field but a ferromagnetic component is frozen-in in decreasing fields (hysteresis loop). The magnetic moment at 5 T is only 4.5 μ_B/Dy atom far from the saturation value (10 μ_B). The neutron diffraction experiments resulted in an incommensurate magnetic structure with a propagation vector $k_Z = 0.2593(4)$ c^* and an additional ferromagnetic contribution [37].

In this respect, our data could be interpreted in the following way: The different Dy positions, i.e., Dy (6*g*) and Dy (4*d*) form two different quasi sub-lattices with two different ordering temperatures $T_C = 120$ K and $T_N = 84$ K as proposed by Semitelou et al. [37]. As the χ' plot shows a wide shoulder (spin glass or cluster glass like behavior) (upper inset in Fig. 10), we tend to believe that the proposed angle (35°) with the *c*-axis and the additional opening angle (20°) of the cone at 2 K are not constant in temperatures below the Néel point but are gradually changing.

The magnetic properties of the boron-containing compound seem to be similar to the pure binary, which is again an indication for rather low boron content in the sample. The paramagnetic data (Fig. 11) result in a $\theta_p = 100$ K and $\mu_{eff} = 10.4\,\mu_B$. The *ac* susceptibility $\chi'(T)$ curve however shows two pronounced maxima at $T = 84$ and 54 K (upper inset in Fig. 11). The magnetization $M(T)$ curve at $B = 0.1$ T shows a maximum around 50 K and the kink at $T \sim 90$ K (upper inset in Fig. 11) corroborates with the above observations. In addition, a ferromagnetic transition is encountered in the $M(T)$ plot at approximately 120 K. The isothermal magnetization $M(B)$ at 80 and 2 K, respectively, are identical with the one observed for the binary compound (lower inset in Fig. 11). Hence, we interpret our finding in the following way: The ordering at $T_C = 120$ K is probably stemming from grains which possibly contain no boron. The boron insertion in binary compounds, e.g. $Ho_3C_{4-x}B_x$ [38], can establish pinning centers (magnetic hardening) or change the type of magnetic order AFM→FM. So the boron atoms in our case might simply act the same way. In the pure binary compound, the canting and opening angles might change gradually whereas the boron atoms might stabilize two particular sets of angles.

The $\rho(T)$ plot shows a metallic character and clearly proves the two transitions at $T_N = 86$ and 50 K in good accord with the magnetic data (Fig. 12). From Eq. (2), the deducted α values are 1.7 for $T < 50$ K and 3.0 for $50 < T < 100$ K.

Ho_5Si_3 and $Ho_5Si_3B_x$: The pure binary phase has been carefully investigated concerning its magnetic properties by Hill et al. (see Table 7) [30]. A plot of the inverse susceptibility versus temperature for $Ho_5Si_3B_x$ gives the value of the paramagnetic moment as 10.8 μ_B, which compares favorably with the theoretical value of 10.6 μ_B per Ho atom and a positive θ_p value of 23 K. This indicates a net ferromagnetic interaction between the holmium atoms. In fact, the *ac* susceptibility measurements down to liquid He temperature confirm a ferromagnetic transition at $T_C = 15$ K (χ' as well as χ'' both show peaked structures, inset in Fig. 13). We note that the magnetic behavior is changed by boron insertion with respect to the pure binary phase: First only one magnetic transition is encountered, second the onset of ferromagnetic ordering is shifted to a higher temperature (Table 7). A similar behavior was earlier encountered upon boron insertion in the compound $Ho_3C_{4-x}B_x$ [38].

The *dc* magnetization plot $M(T)$ at $B = 0.1$ T proves the ferromagnetic transition at $T_C \sim 18$ K (Fig. 14). As the magnetization data were measured in ZFC in increasing temperature, the M values start to rise in the temperature range $2\,K < T < 7$ K. Up to 12 K the magnetization is more or less constant and decreases at higher temperatures due

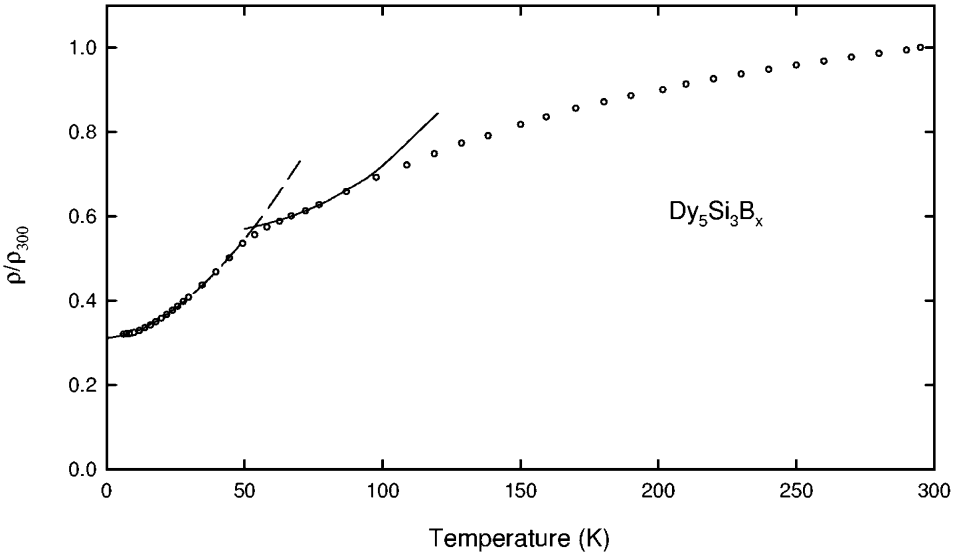

Fig. 12. Electrical resistivity versus temperature for $Dy_5Si_3B_x$. Dashed line calculated after Eq. (2).

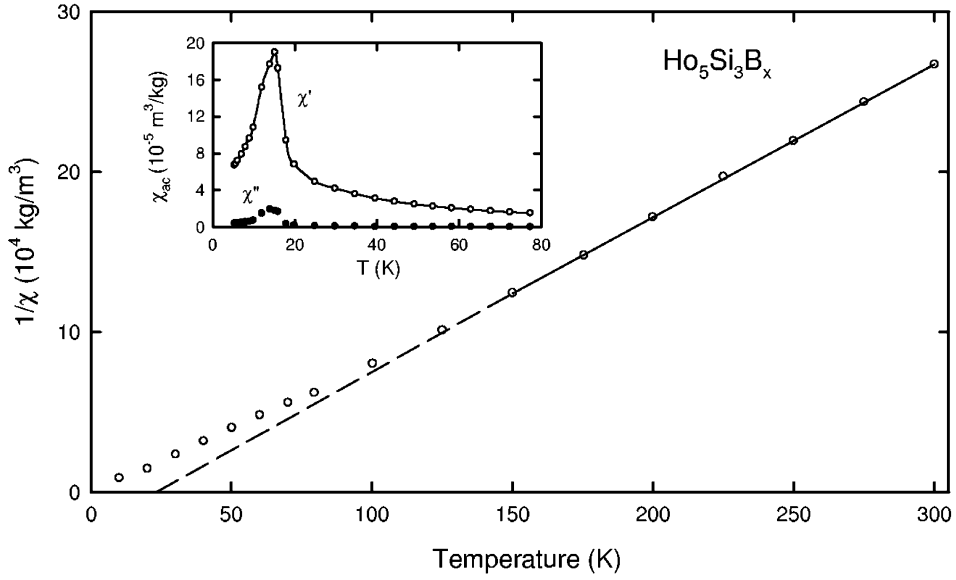

Fig. 13. Reciprocal susceptibility versus temperature for $Ho_5Si_3B_x$. Inset: *ac* susceptibilities versus temperature.

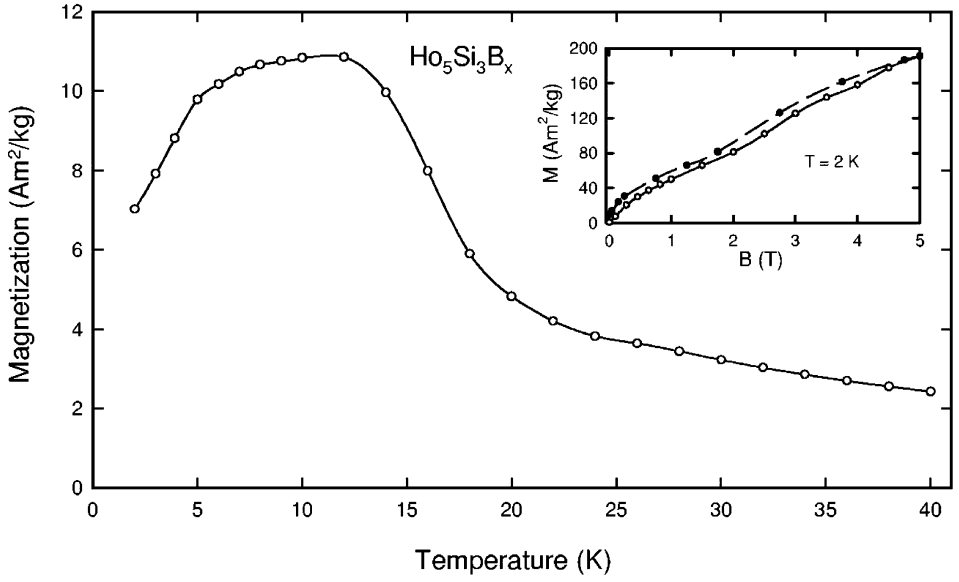

Fig. 14. Magnetization versus temperature in applied field $B = 0.1$ T for $Ho_5Si_3B_x$. Inset: isothermal magnetization versus external field (open circles field up, filled symbols field down).

to the moment disordering. The rise of $M(T)$ at low temperature is often associated with thermal activation of narrow domain walls [34]. The boron atoms thereby act as pinning centers.

The isothermal magnetization $M(B)$ at 2 K (inset in Fig. 14) is similar to the ones presented for the Tb and Dy homologs. In low field up to 2 T, a curvilinear shape is encountered and at 2.5 T as well as 4 T, we observe "metamagnetic-like" inflection points. In decreasing fields (filled symbols), the higher inflection point is vanished, but a hysteresis loop becomes evident. The saturation moment μ_s is equal to 6.2 μ_B at 5 T and 2 K, a value which is far below the ideal value (10 μ_B) for parallel orientation of all moments. Thus, we suspect a similarly complex magnetic structure for $Ho_5Si_3B_x$, as reported for Tb_5Si_3 [29] or Dy_5Si_3 [37].

Er_5Si_3 and $Er_5Si_3B_x$: The magnetic properties of the binary phase have been measured according to the literature [31] and also the antiferromagnetic structure has been investigated [32], where both Er moments in the (4*d*) and (6*g*) positions are lying in the *bc* plane of the hexagonal Mn_5Si_3-type structure, forming an angle of 30° with the *c*-axis.

The inverse susceptibility plot of the ternary phase (Fig. 15) is linear and gives the effective magnetic moment $\mu_{eff} = 9.8\,\mu_B$ in good accord with the free Er^{3+} ion moment (9.6 μ_B) and $\theta_p = 27$ K, reflecting a ferromagnetic-like coupling of the moments. The *ac* susceptibility curves

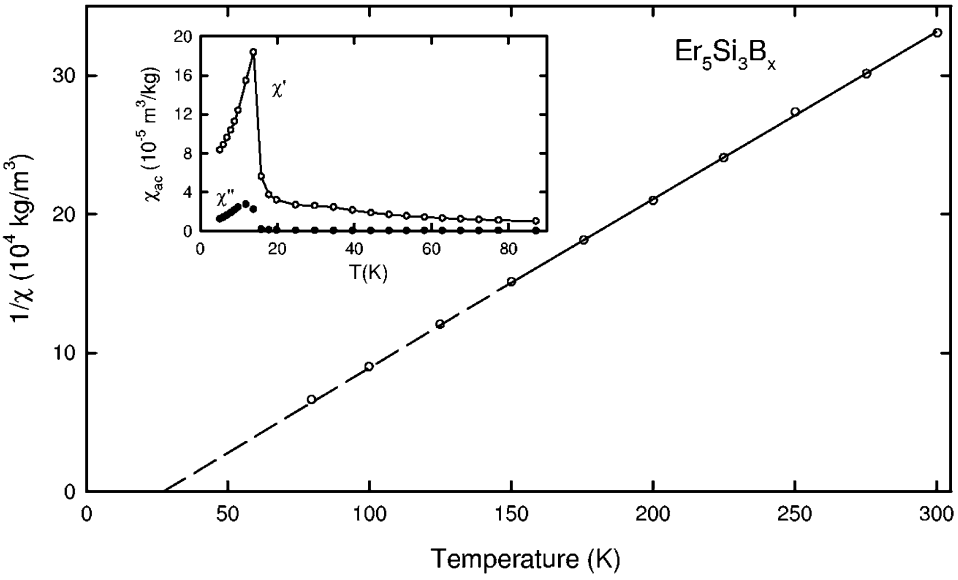

Fig. 15. Reciprocal susceptibility versus temperature for $Er_5Si_3B_x$. Inset: *ac* susceptibilities versus temperature.

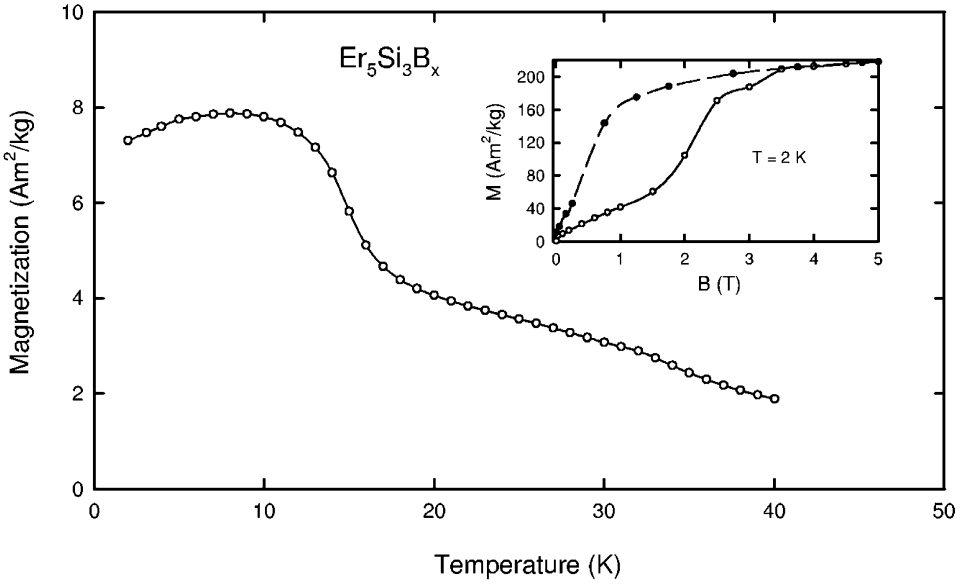

Fig. 16. Magnetization versus temperature in applied field $B = 0.1$ T for $Er_5Si_3B_x$. Inset: isothermal magnetization versus external field (open circles field up, filled symbols field down).

versus temperature show various features: At $T_N = 30$ K a small peak is encountered in the real part χ' but χ'' is temperature independent (inset in Fig. 15). We attribute this to the onset of AFM, which is also proved in the kink of the $M(T)$ curve around 32 K (Fig. 16). In decreasing temperature, a pronounced peak occurs for χ' as well as χ'' at 14 K. We note the strong increase of $M(T)$ below 17 K followed by a broad peak. We conclude that this compound has a ferromagnetic ground state, contrary to the pure binary which is an antiferromagnet. The isothermal magnetizable $M(B)$ plot reveals a wide hysteresis loop (inset in Fig. 16). The initial magnetization rises "linearly" up to 1.5 T, then the $M(B)$ values increase steeply and tend to saturate above 3 T. Consecutively, we observe a second inflection point at 3.2 T and finally saturation is reached above 3.5 T. The saturation moment $\mu_s = 7.3\,\mu_B$ is smaller than the ideal moment $\mu_s = 9\,\mu_B$, but we note that, for polycrystalline bulk samples, this value is never reached for anisotropic ferromagnets. In decreasing fields, the high value of magnetization is frozen in down to about 1 T and then decreases rapidly to a rather small remnant magnetization value. Thus, the coercive field B_{coerc} is estimated to be only 0.1 T. Consequently, we conclude that the magneto-crystalline anisotropy is moderate and the overall ferromagnetic moments reside in the *b,c* plane (easy plane anisotropy) forming an angle with the *c*-axis. The second inflection point of $M(B)$ at 3.2 T could be interpreted as a small change of this angle.

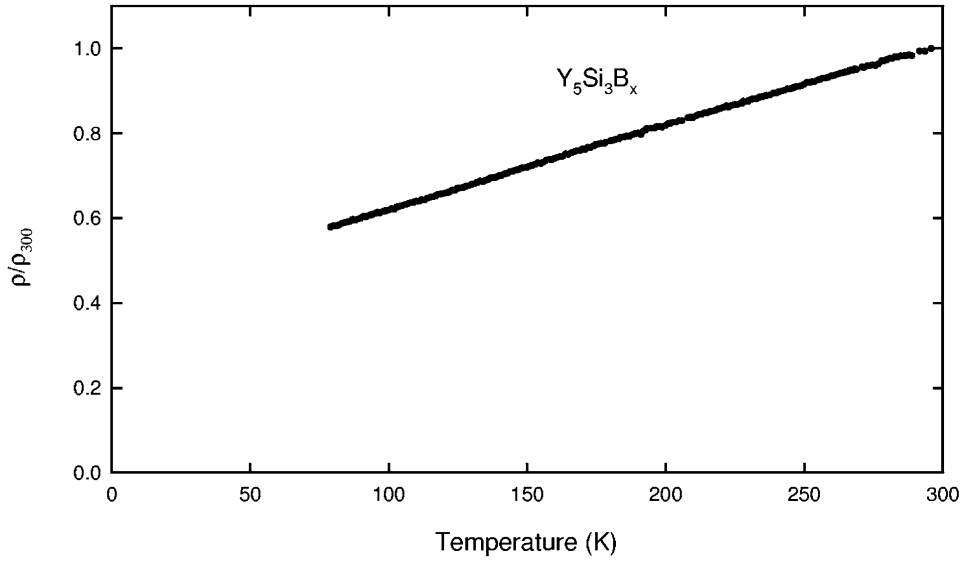

Fig. 17. Electrical resistivity vs temperature for $Y_5Si_3B_x$.

Y_5Si_3 and $Y_5Si_3B_x$: We have measured the electrical resistivities of both samples in a restricted temperature range 80–300 K. Since these samples could not be cut in bar-shaped specimens, only the normalized data ($\rho/\rho_{300\,K}$) were performed. The plot versus temperature of $Y_5Si_3B_x$ shows a linear decrease when the temperature is lowered, proving the metallic character of this compound (Fig. 17) and corroborates with the $\rho(T)$ curve of the binary silicide (not shown).

3.3. Theoretical calculations

Band structure calculations at the DFT level were carried out on $Gd_5Si_3B_x$, varying x from 0 to 1, in order to gain details about the bonding and—if possible—the boron content in the title compounds. The total spin-polarized DOS for $x = 0$, 2/3, and 1 are shown in Fig. 18 *a*, *b* and *c*, respectively. As it can be seen, they look fairly comparable at first sight. For all boron contents, 0, 2/3, and 1, metallic conductivity is expected. No energy gap for any electron count which could indicate a preferred stoichiometry over another one is noticed. Is it due the particular nature of boron which is not very electronegative with respect to Gd and Si, which would lead to some overlapping of occupied boron energy levels and empty metallic bands? Indeed, the boron projected DOS for $x = 2/3$ and 1 indicate some important boron contribution around the Fermi level in resonance with Gd states. Despite that these results are in agreement with the experimental data reported above—RE_5Si_3 and $RE_5Si_3B_x$ are all metallic in character—it does not seem possible at first sight to distinguish between ca. 2/3 or 1 for the boron content in the latter. We just note that the peak of DOS at the Fermi level for $Gd_5Si_3B_{0.667}$ is smaller than that for the binary Gd_5Si_3. This is in accord with the higher resistivity experimentally measured for $Gd_5Si_3B_{0.6}$ with respect to that of Gd_5Si_3 (see above).

We may wonder if there is a relationship between the electron count and the boron content in these phases? Application of the Zintl–Klemm concept [4] leads us to assume RE^{3+}, Si^{4-} and B^{5-} (a high oxidation state for boron indeed). This should preclude the stoichiometric formula Gd_5Si_3B but rather leads to a fractional content of $B_{0.6}$ to satisfy the electronic requirements of boron. Indeed, earlier investigations of some "stuffed" Mn_5Si_3-type phases demonstrated an apparent success of the Zintl–Klemm concept in explaining the relationships between the content of the encapsulated light element and the bonding and physical properties [23]. It was shown experimentally that with Si, C or B, the content in these compounds is generally less than one, but can be equal to one with P or Br for instance [2,6]. For instance, an x value of ca. 0.7 has been proposed for $La_5Ge_3C_x$ [6] and $La_5Ge_3Si_{0.75}$ has clearly been characterized (i.e., consistent with the ideal limit at $x = 0.75$ for a valence compound) [23]. Boron insertion in La_5Ge_3 shows increasing lattice parameters up to 0.6–0.8 in x and becomes constant beyond [6]. The lattice constant variations are too imprecise to conclude about the limiting composition well, but the ideal B need for five electrons would limit stoichiometrically at $x = 0.6$. The electronic conduction properties of these phases are often consistent with this rather simple way of accounting for electrons. La_5Sn_3Br for instance is metallic with electrons remaining in the d band once the electronic requirements of Br are satisfied (i.e., $(La^{3+})_5(Sn^{4-})_3Br^- \cdot 2e$). This was supported both theoretically and experimentally [39]. On the other hand, it was shown that with P, La_5Ge_3P (i.e., $(La^{3+})_5(Ge^{4-})_3P^{3-}$) is semi-conducting with a small band gap confirmed both experimentally and theoretically at the extended Hückel tight-binding level with the Fermi level in a hole of DOS [6]. This was also confirmed by DFT

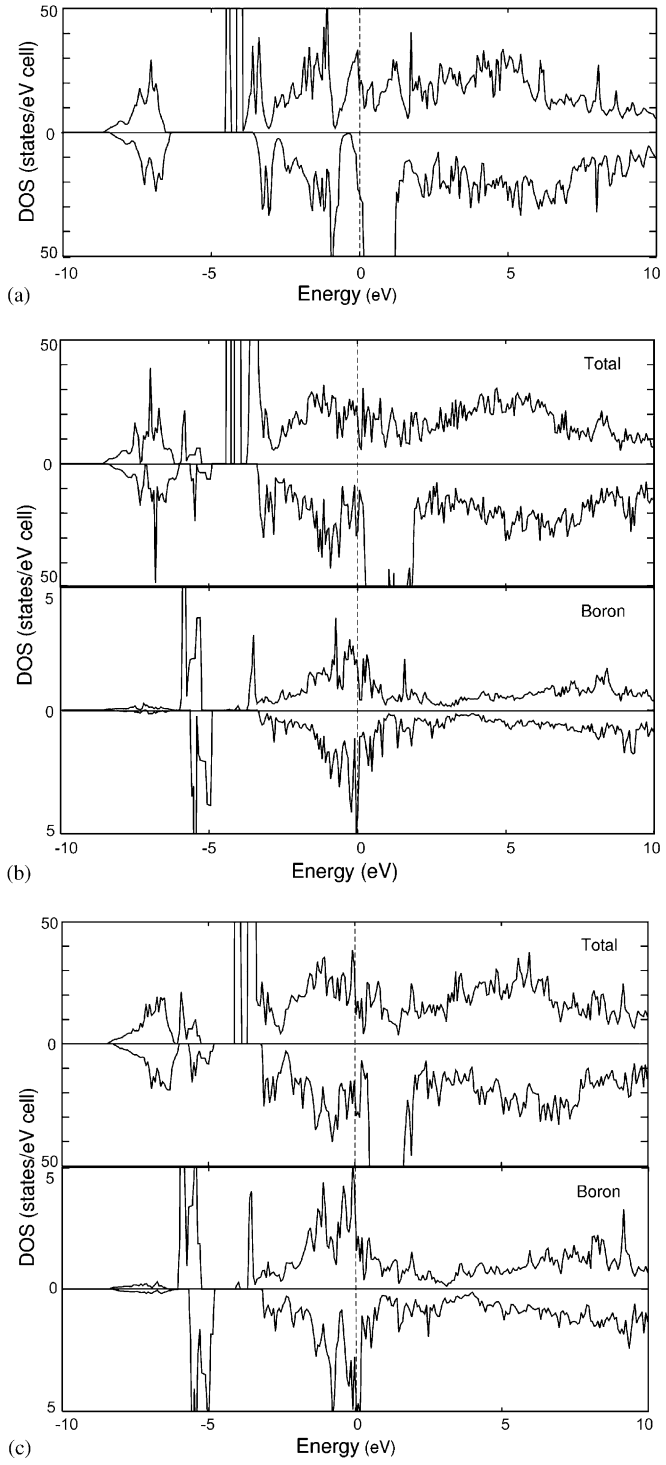

Fig. 18. LMTO–ASA spin-polarized DOS: (a) total DOS for Gd_5Si_3; (b) total and boron projected DOS for $Gd_5Si_3B_{0.667}$; and (c) total and boron projected DOS for Gd_5Si_3B.

calculations that we carried out on La_5Ge_3P. Interestingly, DFT calculations that we performed on the hypothetical phase Gd_5Si_3P, replacing B_x by P, also show a semiconducting behavior with nearly no DOS at the Fermi level.

All these results support the fact that the Zintl–Klemm concept applies to these ternary phases, except for boron since the $RE_5Si_3B_x$ compounds are metallic regardless of x value. Nevertheless, despite of this and though the highest boron content $x = 1$ seems to be experimentally reached for some rare earth metals (see above) we believe that boron gives stoichiometry problems in RE_5Si_3 hosts because there are insufficient electrons to fill the added boron states. With $x = 1$, extra electrons are needed to satisfy the electronic demands of 5- for each isolated boron atom. One way to circumvent this statement would be to create B–B bonding (i.e. to oxidize boron anions). Likewise, as said earlier, the sub-stoichiometric phase $La_5Ge_3Si_{0.75}$ depicts a stuffed Mn_5Si_3 structure, but the fully stoichiometric compound La_5Ge_3Si adopts a Gd_5Si_4-type arrangement with $(Ge/Si)_2$ dimers [23]. Dimerization is evidently forced by the reduced number of electrons introduced by silicon.

The structure $Gd_5Si_3B_x$ was optimized at the DFT level of theory for different contents, 1/3, 2/3, and 1 in order to analyze the possibility of boron–boron pairing. No distortion for 1/3 and 2/3 and distortion for $x = 1$ were expected on the basis of the qualitative electronic pictures implied by the foregoing. Surprisingly, DFT optimization shows the presence of two minima on the potential energy curve for each boron quantity (Table 8). One corresponds to an "undistorted" (U) arrangement with no boron–boron contact (B⋯B separation of ca. 3.2 Å) and the second one to a somewhat "distorted" (D) structure with formation of isolated B_2 dumb-bells (B–B single bond distance of ca. 1.7 Å). Although the energy difference between the U and D structures is rather small, it obviously indicates that boron–boron pairing becomes energetically favorable when the content of boron increases. The U arrangement is slightly preferred by 2 meV per unit cell for low x values ($x = 1/3$) but disfavored for higher x values which are over the valence composition limit of 0.60 ($x = 2/3$ and 1 by 60 and 159 meV, respectively). Examination of the boron projected DOS of the U and D arrangements for $x = 2/3$ and 1 (not shown here) indicates that, as expected, it is more spread out for the latter, reflecting some boron–boron bonding and antibonding states due boron–boron bond formation. This does not mean that the D arrangement should be observed for the stoichiometric composition. It simply says that the U structure seems unlikely for such a composition. Interestingly, we note that for a given x value the structural distortion is accompanied with some increase of the a cell parameter (perpendicular to the quasi-infinite Gd_3Si_3 chains) and some decrease of the c cell parameter (along to the quasi-infinite Gd_3Si_3 chains). This results in a volume cell nearly equal to that of the undistorted arrangement. In contrast to experimental data which show some tiny decrease of the volume cell upon incorporation of boron (see above), some cell increase is computed (Table 8) in line with that experimentally observed for $La_5Ge_3B_x$ [6].

Table 8
Relative energies per cell (E_{REL}, eV), optimized supercell parameters ($a' = a\sqrt{3}$, Å) supercell volume (V, Å^3) and interatomic distances (Å) for energy minima computed for $Gd_5Si_3B_x$

x value	0 (exp)	0 (calcd)	0.333 (calcd) (U)[a]	0.333 (calcd) (D)[a]	0.60 (exp)	0.667 (calcd) (U)	0.667 (calcd) (D)	1.00 (calcd) (U)	1.00 (calcd) (D)
Cell parameters and volume									
a'	14.745	14.800	14.860	14.923	14.732	14.944	15.036	15.005	15.139
c	6.421	6.459	6.459	6.374	6.417	6.389	6.300	6.383	6.230
V	1209.00	1225.32	1234.58	1229.32	1206.15	1235.79	1233.31	1244.68	1236.57
Relative energy per cell									
E_{REL}	—	—	0	+0.002	—	0	−0.060	0	−0.159
Interatomic distances									
B–B	—	—	3.235[b]	1.707	3.209	3.195[b]	1.714	3.192[b]	1.697
							4.585		4.542
Gd1–Gd1	3.210	3.230	3.235	3.187	3.209	3.195	3.150	3.192	3.115
Gd2–Gd2	3.754	3.616	3.612	3.597	3.550	3.767	3.485[c]	3.621	3.491[c]
	3.816	3.846	3.852	3.870	3.808	3.823	4.076	3.815	4.170
Gd2–B	—	—	2.624	2.501	2.603	2.567	2.504	2.630	2.496[c]
				3.092		2.725	3.050		3.076

Experimental cell volumes and interatomic distances of Gd_5Si_3 and $Gd_5Si_3B_{0.6}$ are recalled for comparison.
[a]Undistorted (U) and distorted (D) arrangement.
[b]Averaged.
[c]Limits.

The same results were found for $Lu_5Si_3B_x$ although the stoichiometric composition Lu_5Si_3B seems to be experimentally found (see above). The U structure is slightly more stable than the D one by 3 meV for $x = 1/3$, but less stable by 35 and 100 meV for $x = 2/3$ and 1. Is this result an artifact of the calculations, or is there something real behind? We pushed the study further by replacing boron by carbon, nitrogen or phosphorus for the stoichiometric composition Gd_5Si_3Z. Similarly to boron, geometry optimizations show two energy minima for carbon ($d_{C-C} \approx 1.5$ and 3.2 Å) whereas only one energy minimum is computed for nitrogen or phosphorus at ca. 3.2 Å (Fig. 19). No distortion either is computed for the electron-rich Zr_5Si_3B ($(Zr^{4+})_5(Si^{4-})_3B^{5-} \cdot 3e$) system. Obviously, this is reasonable inasmuch as the host Gd_5Si_3 with isolated Si^{4-} anions can, as said earlier, provide only 3 electrons which are insufficient to completely fill the low-lying valence states of the isolated electron-poor boron and carbon interstitial elements. Boron–boron or carbon–carbon bond is then tentatively formed for the stoichiometric composition to alleviate the lack of host electrons.

The attentive reader may wonder why there is a double energy minimum on the potential energy curve for boron and carbon at short (1.7 Å for boron and 1.5 Å for carbon) and long (ca. 3.2 Å) Z–Z distance? Arguments developed above suggest that we should not observe one minimum at long B···B or C···C separations for the stoichiometric formula. We omitted the host structure in the discussion. The U arrangement is strongly energetically favored for the binary Gd_5Si_3. Stabilization energy is lost when the host lattice is distorted due the variation of Gd–Gd and Gd–Si distances. When the host is fully stuffed by boron or carbon, the two energy minima, U and D, correspond to a

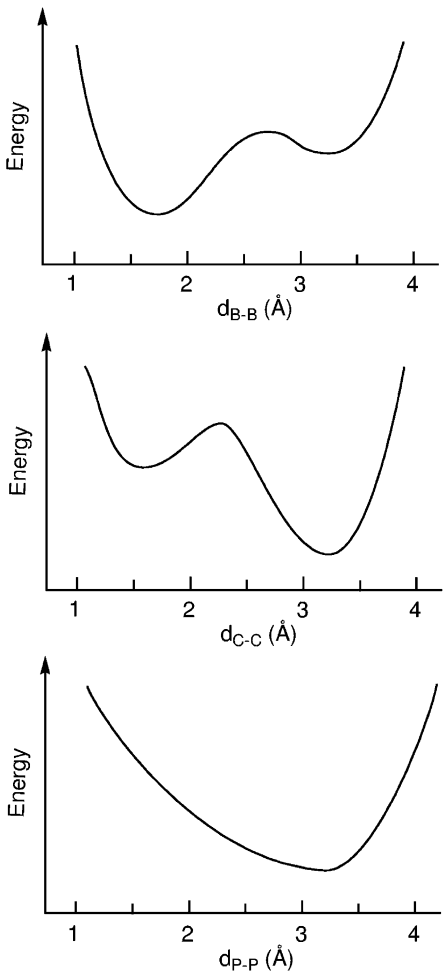

Fig. 19. Schematic potential energy curves as a function of Z–Z distance in Gd_5Si_3Z: Z = B (top), C (middle) and P (bottom).

compromise between opposite forces: At long Z–Z separation, the stabilizing energy of the host prevails over the destabilizing energy of isolated interstitial elements, but at short Z–Z distance, the reverse is at work, the stabilizing energy corresponding to Z–Z bond formation overtakes the destabilization energy of the distorted host lattice. The lack of stabilizing force for Z–Z bond formation does not countervail the destabilizing energy of the distorted host lattice in the case of electron-rich interstitials (nitrogen or phosphorus) and therefore only one energy minimum is computed corresponding to the U arrangement.

4. Conclusion

To summarize, exploration of some *RE*–B–Si phase diagrams has led to the discovery of boron-interstitial phases $RE_5Si_3B_x$ which derive from the Mn_5Si_3-type binary phases RE_5Si_3 and which consist of isolated Si atoms, isolated metal atoms and metal octahedra in which are encapsulated the B atoms. According to X-ray crystal structure determinations, the content of boron may vary roughly from 0.60 (Y, Gd) up to ca. 1 (Dy, Ho or Lu) within the limits of errors of measurements. A comparison of their physical properties to those measured for the binary phase RE_5Si_3 indicate that they differ substantially. Although they are all metallic, the ternary phases display higher resistivity and some diminution of the exchange magnetic interactions with respect to those of the related binaries. Simple charge-balancing should preclude the stoichiometric formula RE_5Si_3B but should rather lead to a fractional content of 0.6 to satisfy the electronic requirements of boron as experimentally observed for rare-earth metals. DFT calculations carried out on some $RE_5Si_3Z_x$ systems for different Z atoms, B, C, N or P and different x amounts from 0 to 1 give some support to this statement. The metallic nature of $RE_5Si_3B_x$ stems from the overlap between the *RE* and B states around the Fermi level.

Supporting information available

Further details on the crystal structure investigations may be obtained from the Fachinformationszentrum Karlsruhe, 76344 Eggenstein-Leopoldshafen, Germany (fax: (49) 7247-808-666; e-mail: crysdata@fiz.karlsruhe.de), on quoting the depository number from CSD-415740 up to CSD-415747 for $Y_5Si_3B_{0.65}$, Y_5Si_3, Ho_5Si_3B, Ho_5Si_3, $Gd_5Si_3B_{0.60}$, Gd_5Si_3, Dy_5Si_3B, Dy_5Si_3, respectively and CSD-415737 for Lu_5Si_3B, the name of the authors, and citation of the paper.

Acknowledgments

The authors acknowledge support from the Austrian (ÖAD)—French (MAE) Amadeus exchange program under projects 9/2005 (Austria) and 08940YH (France). Thanks are expressed to Dr. T. Roisnel (CDIFX, Université de Rennes 1) for X-ray intensity data collection, J.-C. Jégaden, J. Le Lannic (CMEBA, Université de Rennes 1) and M. Bohn (IFREMER, Brest) for their assistance in SEM and EPMA studies, as well as Drs. C.-M. Fang and E. Furet for computational assistance. The authors thank also the Pôle de Calcul Intentif de l'Ouest (PCIO) of the University of Rennes, the Institut de Développement et de Ressources en Informatique Scientifique (IDRIS-CNRS), and the Centre Informatique National de l'Enseignement Supérieur (CINES) for computing facilities.

References

[1] B. Aronsson, Acta Chem. Scand. 14 (1960) 1414.
[2] J.D. Corbett, E. Garcia, A.M. Guloy, W.M. Hurng, Y.U. Kwon, E.A. Leon-Escarmilla, Chem. Mater. 10 (1998) 2824 and references therein.
[3] (a) H. Schachner, E. Cerwenka, H. Nowotny, Monatsh. Chem. 85 (1954) 241;
(b) H. Nowotny, B. Lux, H. Kudielka, Monatsh. Chem. 87 (1956) 447;
(c) W. Jeitschko, H. Nowotny, F. Benesovsky, Monatsh. Chem. 95 (1964) 1242;
(d) W. Jeitschko, W. Rieger, H. Nowotny, F. Benesovsky, Monatsh. Chem. 95 (1964) 1413;
H. Nowotny, F. Benesovsky, in: P.S. Rudman, J. Stringer, R.I. Jaffee (Eds.), Phase Stability in Metals and Alloys, McGraw-Hill, New York, 1966, p. 319 (Note that the label *Nowotny phases* originally refers to ternaries phases for which the binary was thought to be unstable).
[4] (a) E. Zintl, Angew. Chem. 1 (1939) 52;
(b) W. Klemm, Proc. Chem. Soc. London (1958) 329.
[5] I. Mayer, I. Felner, J. Less-Common Met. 37 (1974) 171.
[6] A. Guloy, J.D. Corbett, Inorg. Chem. 32 (1993) 3532.
[7] A.J. Thom, V.G. Young, M. Akinc, J. Alloys Compds. 296 (2000) 59.
[8] (a) V. Babizhetskyy, J. Roger, S. Députier, R. Guérin, R. Jardin, J. Bauer, K. Hiebl, C. Jardin, J.-Y. Saillard, J.-F. Halet, Angew. Chem. Int. Ed. 43 (2004) 1979;
(b) J. Roger, V. Babizhetskyy, S. Cordier, J. Bauer, K. Hiebl, L. Le Pollès, S.E. Ashbrook, J.-F. Halet, R. Guérin, J. Solid State Chem. 178 (2005) 1851.
[9] J. Emsley, The Elements, Oxford University Press, Oxford, 1989.
[10] (a) V. Babizhetskyy, J. Roger, S. Députier, R. Jardin, J. Bauer, R. Guérin, J. Solid State Chem. 177 (2004) 415;
(b) M. Ben Yahia, J. Roger, X. Rocquefelte, R. Gautier, J. Bauer, R. Guérin, J.-Y. Saillard, J.-F. Halet, J. Solid State Chem. (2006) (in press). Available online 2 February 2006.
[11] COLLECT: KappaCCD software, Nonius BV, Delft, The Netherlands, 1998.
[12] Z. Otwinowski, W. Minor, in: C.W. Carter Jr., R.M. Sweet (Eds.), Methods in Enzymology, vol. 276, Academic Press, New York, 1997, p. 307.
[13] R.H. Blessing, Acta Crystallogr. A 51 (1995) 33.
[14] A. Altomare, M.C. Burla, M. Camalli, B. Carrozzini, G.L. Cascarano, C. Giacovazzo, A. Guagliardi, A.G.G. Moliterni, G. Polidori, R. Rizzi, Acta Crystallogr. A 32 (1999) 115.
[15] G.M. Sheldrick, SHELXL-97, Program for the Refinement of Crystal Structures, University of Göttingen, Germany, 1997.
[16] K. Brandenburg, Diamond, Version 2.0, 1998.
[17] (a) O.K. Andersen, Phys. Rev. B 12 (1975) 3060;
(b) O.K. Andersen, Europhys. News 12 (1981) 4;
(c) O.K. Andersen, in: P. Phariseau, W.M. Temmerman (Eds.), The Electronic Structure of Complex Systems, Plenum Publishing Corporation, New York, 1984;
(d) O.K. Andersen, O. Jepsen, Phys. Rev. Lett. 53 (1984) 2571;
(e) O.K. Andersen, O. Jepsen, M. Sob, in: M. Yussouf (Ed.), Electronic Band Structure and its Application, Springer, Berlin, 1986;
(f) H.L. Skriver, The LMTO Method, Springer, Berlin, 1984.

[18] U. von Barth, L. Hedin, J. Phys. C 5 (1972) 1629.
[19] P.E. Blöchl, O. Jepsen, O.K. Andersen, Phys. Rev. B 49 (1994) 16223.
[20] (a) G. Kresse, J. Hafner, Phys. Rev. B 47 (1993) 558;
(b) G. Kresse, Hafner, J. Phys. Rev. B 49 (1994) 14251;
(c) G. Kresse, J. Furthmuller, Comput. Mater. Sci. 6 (1996) 15;
(d) G. Kresse, J. Furthmuller, Phys. Rev. B 54 (1996) 11169.
[21] (a) P.E. Blöchl, Phys. Rev. B 50 (1994) 17953;
(b) G. Kresse, D. Joubert, Phys. Rev. B 59 (1999) 178.
[22] J.P. Perdew, K. Burke, M. Ernzerhof, Phys. Rev. Lett. 77 (1996) 3865 (Erratum, Phys. Rev. Lett. 78 (1997) 1396).
[23] A. Guloy, J.D. Corbett, J. Solid State Chem. 178 (2005) 1112.
[24] K.S.V.L. Narasimkam, H. Steinfink, E.V. Ganaphaty, J. Appl. Phys. 40 (1) (1969) 51.
[25] E.V. Ganaphaty, K. Kugimiya, H. Steinfink, D.I. Tchernev, J. Less-Common Met. 44 (1976) 245.
[26] V.N. Safonov, P.V. Gel'd, N.I. Sychev, G.I. Kalishevich, Yu.A. Vereshchagin, Sov. Phys. Solid State 25 (9) (1983) 1604.
[27] F. Canepa, S. Cirafici, F. Merlo, A. Palenzona, J. Magn. Magn. Mater. 118 (1–2) (1993) 182.
[28] F. Canepa, S. Cirafici, M. Napoletano, J. Alloys Compds. 335 (2002) L1.
[29] I.P. Semitelou, H. Konguetsof, J.K. Yakinthos, J. Magn. Magn. Mater. 79 (1989) 131.
[30] P. Hill, L.L. Miller, J. Appl. Phys. 87 (9) (2000) 6034.
[31] V.N. Safonov, P.V. Gel'd, Yu.A. Vereshchagin, G.I. Kalishevich, Sov. Phys. Solid State 25 (11) (1983) 3471.
[32] I.P. Semitelou, J.K. Yakinthos, E. Roudaut, J. Phys. Chem. Solids 56 (7) (1995) 891.
[33] F. Holtzberg, R.J. Gambino, T.R. McGuire, J. Phys. Chem. Solids 28 (1967) 2283.
[34] K.H.J. Buschow, in: E.P. Wohlfarth (Ed.), Ferromagn. Mater., vol. 1, North-Holland, Amsterdam, 1980, p. 283.
[35] G.T. Meaden, Contemp. Phys. 12 (1971) 313.
[36] A.R. MacIntosh, Phys. Lett. 4 (1963) 140.
[37] I.P. Semitelou, J.K. Yakinthos, J. Magn. Magn. Mater. 265 (2003) 152.
[38] E. Bidaud, K. Hiebl, J. Bauer, J. Alloys Compd. 279 (1998) 97.
[39] C. Zheng, Hj Mattausch, A. Simon, J. Alloys Compd. 347 (2002) 79.